VERSITA

Barrier infrared detectors

P. MARTYNIUK*, M. KOPYTKO, and A. ROGALSKI

Institute of Applied Physics, Military University of Technology, 2 Kaliskiego Str., 00–908 Warsaw, Poland

In 1959, Lawson and co-workers publication triggered development of variable band gap $Hg_{1-x}Cd_xTe$ (HgCdTe) alloys providing an unprecedented degree of freedom in infrared detector design. Over the five decades, this material system has successfully fought off major challenges from different material systems, but despite that it has more competitors today than ever before. It is interesting however, that none of these competitors can compete in terms of fundamental properties. They may promise to be more manufacturable, but never to provide higher performance or, with the exception of thermal detectors, to operate at higher temperatures.

In the last two decades a several new concepts of photodetectors to improve their performance have been proposed including trapping detectors, barrier detectors, unipolar barrier photodiodes, and multistage detectors. This paper describes the present status of infrared barrier detectors. It is especially addressed to the group of III–V compounds including type-II superlattice materials, although HgCdTe barrier detectors are also included. It seems to be clear that certain of these solutions have merged as a real competitions of HgCdTe photodetectors.

1. Introduction

At present HgCdTe is the most widely used variable gap semiconductor for infrared (IR) photodetectors [1]. The specific advantages of HgCdTe are the direct energy gap, ability to obtain both low and high carrier concentrations, high mobility of electrons and low dielectric constant. The extremely small change of lattice constant with composition makes it possible to grow high quality layers and heterostructures. HgCdTe can be used for detectors operated at various modes (photoconductors, photodiodes and MIS detectors), and can be optimized for operation at the extremely wide range of the IR spectrum (from visible region to 30 μm) and at temperatures ranging from that of liquid helium to room temperature.

The main motivations to replace HgCdTe are technological problems with this material. One of them is a weak Hg-Te bond, which results in bulk, surface and interface instabilities. Uniformity and yield are still issues especially in the LWIR spectral range. Nevertheless, HgCdTe remains the leading semiconductor for IR detectors.

Recently, there has been a considerable progress towards the materials' development and device design innovations. In particular, significant advances have been made during the last two decades in the band-gap engineering of various compound semiconductors that has led to new detector architectures. New emerging strategies include barrier structures such as nBn detector, low-dimensional solids

[especially type-II superlattices (T2SLs)] with lower generation-recombination leakage mechanisms, photon trapping detectors and multi-stage/cascade infrared devices.

This review paper presents approaches, materials, and device structures of the infrared barrier detectors. The intent is to concentrate on device approaches that are having the most impact today in the main stream of infrared detector technologies. The secondary aim is to outline the evolution of detector technologies showing why certain device designs and architecture have emerged as more useful today also as alternative technologies competitive to HgCdTe ternary alloy.

2. Concept of barrier infrared detector

Historically, the first barrier detector was proposed by A.M. White in 1983 as a high impedance photoconductor [2]. It postulates an n-type heterostructure with a narrow gap absorber region coupled to a thin wide bandgap layer, followed by a narrow bandgap contact region. The concept assumes almost zero valence band offset approximation throughout the heterostructure, what allows for a flow of only minority carriers in a photoconductor. Little or no valence band offset was difficult to realize using standard infrared detector materials such as InSb and HgCdTe. Situation has changed dramatically in the middle of the first decade of XXI century after introducing of 6.1 Å III-V material detector family and when the first high-performance detectors and FPAs were demonstrated [3–5]. Introducing of unipolar barriers in various designs based on T2SLs drasti-

*e-mail: pmartyniuk@wat.edu.pl

⚛ Springer

cally changed the architecture of infrared detectors [6]. In general, unipolar barriers are used to implement the barrier detector architecture for increasing the collection efficiency of photogenerated carriers and reducing dark current generation without inhibiting photocurrent flow. The ability to tune the positions of the conduction and valence band edges independently in a broken-gap T2SL is especially helpful in the design of unipolar barriers.

The term "unipolar barrier" was coined to describe a barrier that can block one carrier type (electron or hole) but allows for the un-impeded flow the other (see Fig. 1). Between different types of barrier detectors the most popular is nBn detector shown in Fig. 1. The n-type semiconductor on one side of the barrier constitutes a contact layer for biasing the device, while the n-type narrow-bandgap semiconductor on the other side of the barrier is a photon--absorbing layer whose thickness should be comparable to the absorption length of light in the device, typically several microns. The same doping type in the barrier and active layers is key to maintaining low, diffusion limited dark current. The barrier should be carefully engineered. It must be nearly lattice matched to the surrounding material and have a zero offset in the one band and a large offset in the other. It should be located near the minority carrier collector and away from the region of optical absorption. Such barrier arrangement allows photogenerated holes to flow to the

contact (cathode) while majority carrier dark current, re-injected photocurrent, and surface current are blocked (see bottom right side of Fig. 1). So, the nBn detector is designed to reduce dark current (associated with SRH processes) and noise without impending photocurrent (signal). In particular, the barrier serves to reduce surface leakage current. Spatial makeups of the various current components and barrier blocking in nBn detector is shown in the bottom right side of Fig. 1 [7].

The nBn detector is essentially a photoconductor with unity gain, due to the absence of majority carrier flow, and in this respect is similar to a photodiode – the junction (space charge region) is replaced by an electron blocking unipolar barrier (B), and that the p-contact is replaced by an n-contact. It can be stated, that the nBn design is a hybrid between photoconductor and photodiode.

Figure 2 shows a typical Arrhenius plot of the dark current in a conventional diode and in nBn detector. The diffusion current typically varies as $T^3 \exp(-E_{g0}/kT)$, where E_{g0} is the band gap extrapolated to zero temperature, T is the temperature, and k is the Boltzman's constant. The generation-recombination current varies as $T^{3/2} \exp(-E_{g0}/2kT)$ and is dominant by the generation of electrons and holes by SRH traps in the depletion region. Because in nBn detector there is no depletion region, the generation-recombination contribution to the dark current from the photon-absorbing
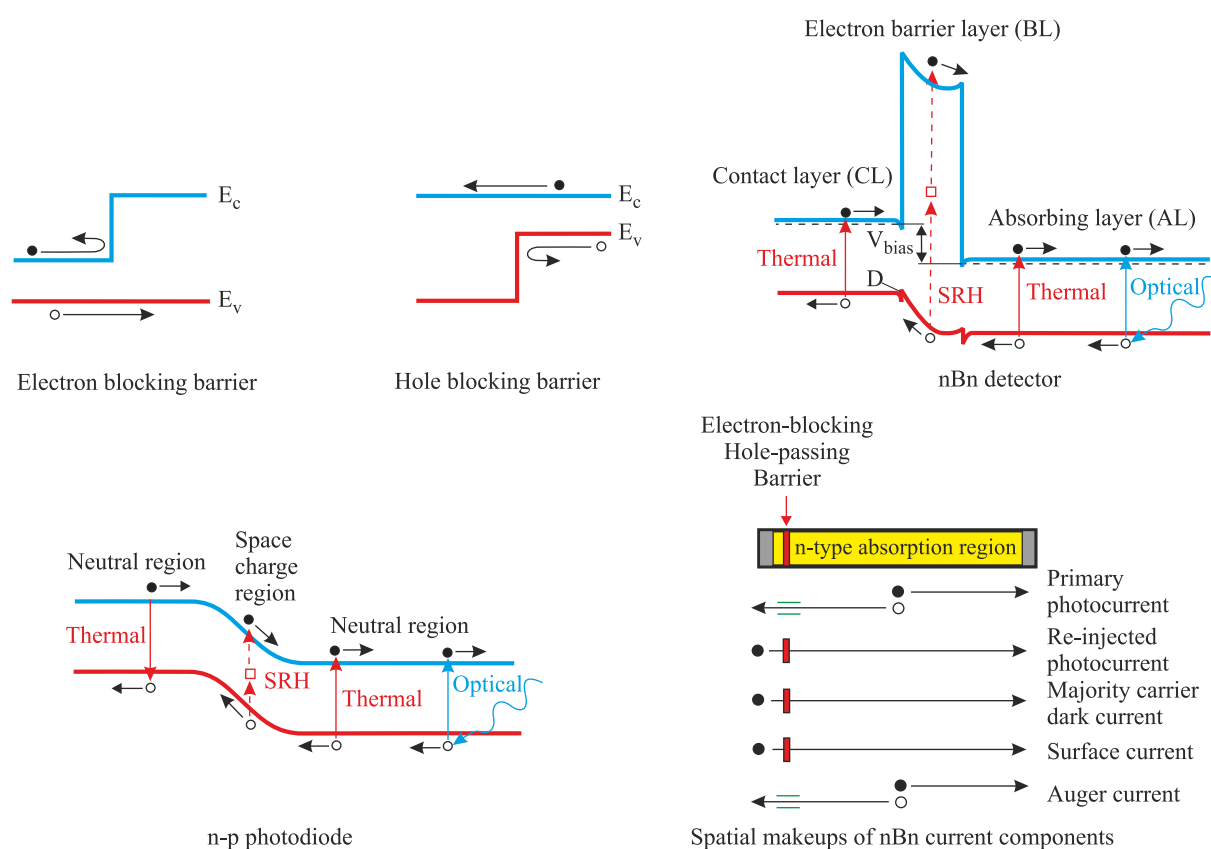

Fig. 1. Illustrations of electron- and hole-blocking unipolar barriers, band gap diagram of nBn barrier detector (the valence-band offset, Δ, is shown explicitly) and p-n photodiode. Bottom right side of nBn barrier detector shows spatial makeups of the various current components and barrier blocking (adapted after Ref. 7).

layer is totally suppressed. The lower portion of Arrhenius plot for the standard photodiode has a slope that is roughly half that of the upper portion. The solid line (nBn) is an extension of the high temperature diffusion limited region to temperatures below T_c. T_c is defined as the crossover temperature at which the diffusion and generation-recombination currents are equal. In a low-temperature region, nBn detector offers two important advantages. First, it should exhibit a higher signal-to-noise ratio than a conventional diode operating at the same temperature. Second, it will operate at a higher temperature than a conventional diode with the same dark current. This is depicted by a horizontal green dashed line in Fig. 2.

Absence of a depletion region offers a way for materials with relatively poor SR lifetimes, such as all III–V compounds, to overcome the disadvantage of large depletion dark currents.

The operating principles of the nBn and related detectors have been described in detail in the literature [4–12]. While the idea of nBn design was originated with bulk InAs materials [4], its demonstration using T2SL based materials facilitates the experimental realization of the barrier detector concept with better control of band edge alignments [6].

Wide family of barrier detectors has been considered by Klipstein *et al.* [13]. They can be divided in two groups: XB_nn and XB_pp detectors (see Fig. 3). In the case of the first group, all have the same n-type B_nn structural unit, but used different contact layers (X), where either the doping, material, or both are varied. If we take, e.g., C_pB_nn and nB_nn devices, C_p is the p-type contact made from a different material to the active layer, whereas n is the n-type contact made from the same material. In the case of pB_nn structure, the p-n junction can be located at the interface between the
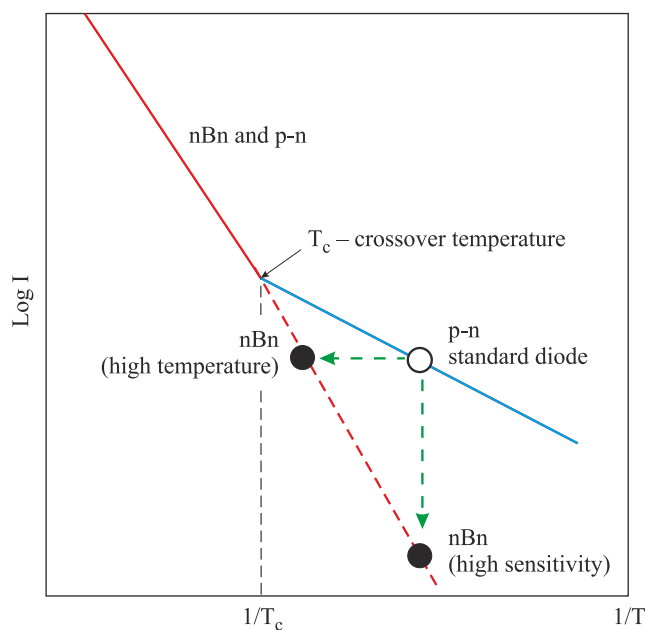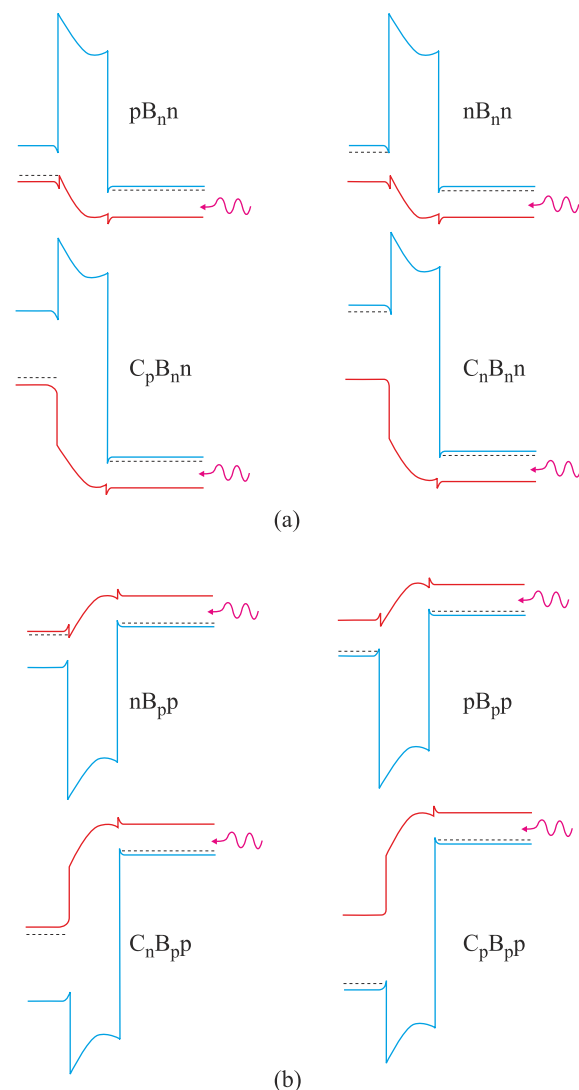

(a)

(b)

Fig. 3. Schematic band profile configurations under operating bias for XB_nn (a) and XB_pp (b) barrier detector families. In each case the contact layer (X) is on the left, and infrared radiation is incident onto the active layer on the right. When *X* is composed of the same material as the active layer, both layers have the same symbol (denoting the doping type), otherwise it is denoted as C (with the doping type as a subscript) (after Ref. 13).

heavily doped p-type material and the lower-doped barrier, or within the lower-barrier itself. Our barrier detector family also has p-type members, designated as XB_pp, which are polarity-reversed versions of the n-type detectors. The pBp architecture should be employed when the surface conduction of the materials is p-type and must be used a p-type absorbing layer. The last structure can be realized using, e.g., a p-type InAs/GaSb T2SLs as the absorbing layer [14, 15]. So called pMp device consists of two p-doped superlattice active region and a thin M-structure with higher energy barrier. The band gap difference between superlattice M structure falls in the valence band, creating a valence band barrier for the majority holes in a p-type semiconductor.

Fig. 2. Schematic Arrhenius plot of the dark current in a standard diode and in nBn device (adopted after Ref. 8).

Unipolar barriers can also be inserted into a conventional p-n photodiode architecture [7,16]. There are two possible locations into which a unipolar barrier can be implemented: outside of depletion layer in the p-type layer or near the junction, but at the edge of the n-type absorbing layer (see Fig. 4). In dependence of barrier placement, different dark current components are filtered. For example, placing the barrier in the p-type layer blocks surface current, but currents due to diffusion, generation-recombination, trap-assisted tunnelling, and band-to-band tunnelling cannot be blocked. If the barrier is placed in the n-type region, the junction generated currents and surface currents are effectively filtered out. The photocurrent shares the same spatial makeup as the diffusion current, what is shown in Fig. 5.

Unipolar barriers can significantly improve the performance of infrared photodiodes, what is shown in Fig. 7 for InAs material system. In InAs, $AlAs_{0.18}Sb_{0.82}$ is an ideal electron blocking unipolar barrier material. Theoretical predictions suggests that valence band offset (VBO) should be less than k_BT for barrier composition in the range of $0.14 < y < 0.18$. Figure 6 compares the temperature dependent R_0A product data for an n-side unipolar barrier photodiode with that of a conventional p-n photodiode. The unipolar barrier photodiode shows performance near Rule 07
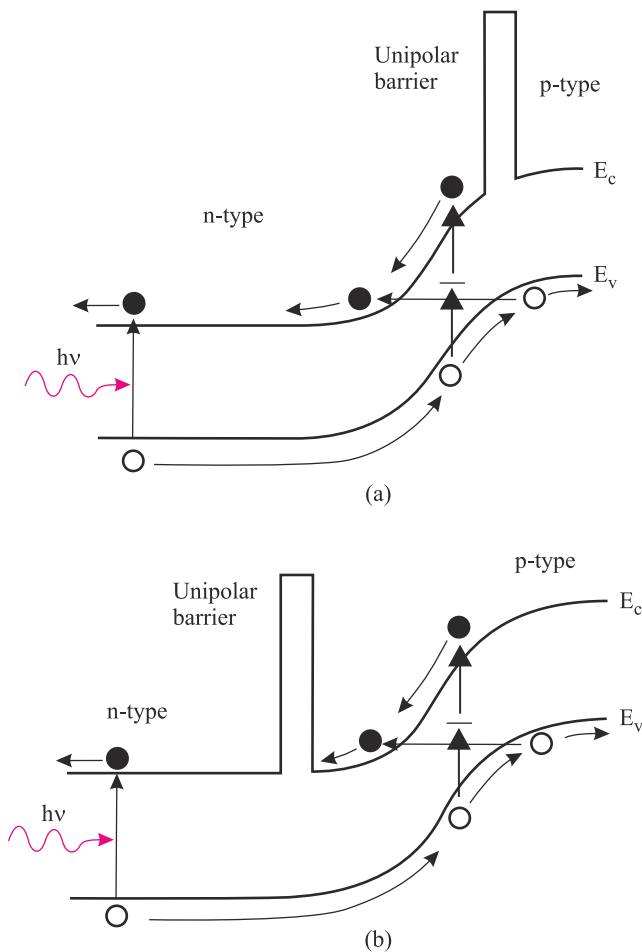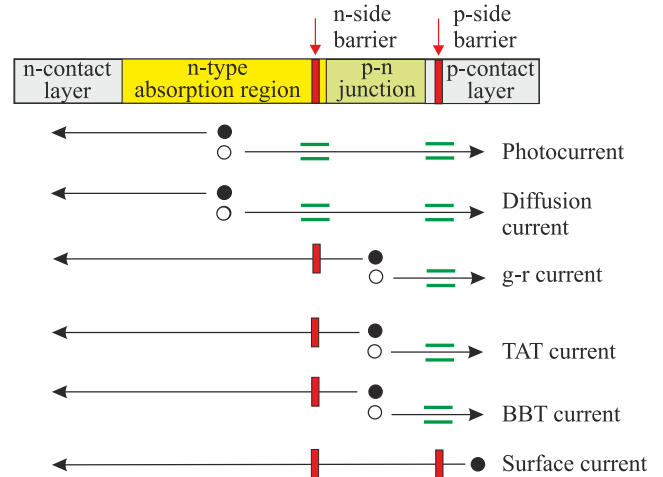

Fig. 5. Placing the barrier in a unipolar barrier photodiode results in the filtering of surface currents and junction related currents. Diffusion current is not filtered because it shares the same spatial makeup as the photocurrent (after Ref. 7).
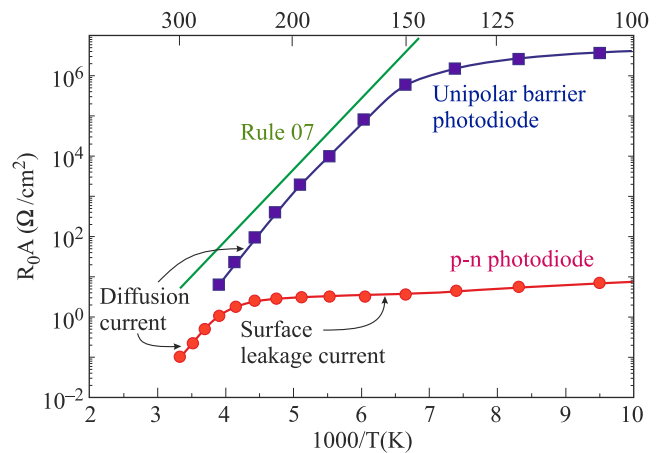

Fig. 6. R_0A product of a conventional InAs photodiode and comparable n-side barrier photodiode (after Ref. 16).

with activation energy near the bandgap of InAs indicating diffusion limited performance and six orders of magnitude higher R_0A value in low temperature range than that of conventional p-n junction.

3. Material considerations for barrier infrared detectors

The barrier detector can be implemented in different semiconductor materials. Absence of a depletion region offers a way for materials with relatively poor SR lifetimes, such as all III-V compounds, to overcome the disadvantage of large depletion dark currents. Its practical application has been demonstrated in InAs [4,7,16], InAsSb [8,10,13,17,18] InAs/GaSb T2SLs [5,9,14,15] and recently, also in HgCdTe ternary alloy [19,20].

The main requirement which must be met to construct the barrier detector structure is "zero" band offset in a pro-

Fig. 4. Band diagrams of a p-side (a) and an n-side (b) unipolar photodiode under bias (after Ref. 7).

per band depending on carrier type which is to be blocked. Material systems where a large conduction band offset is not realizable, the pBn architecture may be preferable. The traditional nBn structure requires bias to operate. Once zero bias operation is crucial, again pBn architecture may be used [21]. The large band offset requirement in one band and zero offset in the other is not the only one requirement to fabricate a barrier detector; the lattice matching between surrounding materials is also significant.

Table 1 presents some physical properties of semiconducting families used in fabrication of infrared photodetectors. All compounds have diamond (D) or zincblende (ZB) crystal structure. Moving across the table from the left to the right, there is a trend in change of chemical bond from the covalent group IV-semiconductors to more ionic II-VI semiconductors with increasing of the lattice constant. The chemical bonds become weaker and the materials become softer what is reflected by the values of the bulk. The materials with larger contribution of covalent bound are more mechanically robust, which leads to better manufacturability. This is evidenced in the dominant position of silicon in electronic materials and GaAs in optoelectronic ones. On the other hand, the band gap energy of semiconductors on the right side of the table tends to have smaller values. Due to their direct band gap structure, strong band-to-band absorption leading to high quantum efficiency is observed (e.g., in InSb and HgCdTe).

Currently among the materials used in fabrication barrier detectors, 6.1 Å III-V family plays the decisive role by offering high performance connected with high design flexibility, direct energy gaps and strong optical absorption. The three semiconductors: InAs, GaSb and AlSb form an approximately lattice-matched set around 6.1 Å, with the room temperature energy gaps ranging from 0.36 eV (InAs) to 1.61 eV (AlSb) [22]. Like other semiconductor alloys, they are of interest principally for their heterostructures, especially combining InAs with the two antimonides and their alloys. This combination offers band lineups that are drastically different from those of more widely studied AlGaAs system, and the lineups are one of the principal reasons for interest in the 6.1 Å family. The most exotic lineup is that of InAs/GaSb heterojunctions, for which it was found in 1977 by Sakaki *et al.* [23] and that they exhibit a broken gap lineup: at the interface the bottom of a conduction band of InAs lines up below the top of the valence band of GaSb with a break in the gap of about 150 meV. In such a heterostructure, with partial overlapping of the InAs conduction band with the GaSb-rich solid solution valence band, electrons and holes are spatially separated and localized in self-consistent quantum wells formed on both sides of the heterointerface. This leads to unusual tunnelling-assisted radiative recombination transitions and novel transport properties. As illustrated in Fig. 7, with the availability of type-I (nested, or straddling), type-II staggered, and type-II broken

Table 1. Selected properties of common families of semiconductors used in fabrication of infrared photodetectors.

	Si	Ge	GaAs	AlAs	InP	InGaAs	AlInAs	InAs	GaSb	AlSb	InSb	HgTe	CdTe
Group	IV	IV	III–V	III–V	III–V	III–V	III–V	III–V	III–V	III–V	III–V	II–VI	II–VI
Lattice constant (Å)/structure	5.431 (D)	5.658 (D)	5.653 (ZB)	5.661 (ZB)	5.870 (ZB)	5.870 (ZB)	5.870 (ZB)	6.058 (ZB)	6.096 (ZB)	6.136 (ZB)	6.479 (ZB)	6.453 (ZB)	6.476 (ZB)
Bulk moduls (Gpa)	98	75	75	74	71	69	66	58	56	55	47	43	42
Band gap (eV)	1.124 (id)	0.660 (id)	1.426 (d)	2.153 (id)	1.350 (d)	0.735 (d)		0.354 (d)	0.730 (d)	1.615 (id)	0.175 (d)	0.141 (d)	1.475 (d)
Electron effective mass	0.26	0.39	0.067	0.29	0.077	0.041		0.024	0.042	0.14	0.014	0.028	0.090
Hole effective mass	0.19	0.12	0.082(L) 0.45(H)	0.11(L) 0.40(H)	0.12(L) 0.55(H)	0.05(L) 0.60(H)		0.025(L) 0.37(H)	0.4	0.98	0.018(L) 0.4(H)	0.40	0.66
Electron mobility (cm^2/Vs)	1450	3900	8500	294	5400	13800		3×10^4	5000	200	8×10^4	26500	1050
Hole mobility (cm^2/Vs)	505	1900	400	105	180			500	880	420	800	320	104
Electron saturation velocity (10^7 cm/s)	1.0	0.70	1.0	0.85	1.0			4.0			4.0		
Thermal cond. (W/cmK)	1.31	0.31	0.5		0.7			0.27	0.4	0.7	0.15		0.06
Relative dielectric constant	11.9	16.0	12.8	10.0	12.5			15.1	15.7	12.0	17.9	21	10.2
Substrate	Si,Ge		GaAs			InP		InAs,GaSb			InSb	CdZnTe,GaAs,Si	
MW/LW detection mechanism	Heterojunction internal photoemission		QWIP,QDIP		QWIP			Bulk (MW) Superllatice (MW/LW) Band-to-band (B-B)			Bulk B-to-B	Bulk Band-to-band	

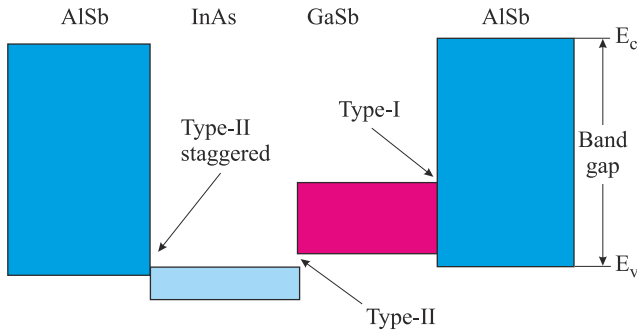D – diamond, ZB – zincblende, id – indirect, d – direct, L – light hole, H – heavy hole

Fig. 7. Schematic illustration of the energy band alignment in the nearly lattice matched InAs/GaSb/AlSb material system. Three types of band alignment are available in this material system: type-I (nested) band alignment between GaSb and AlSb, type-II staggered alignment between InAs and AlSb, and type-II broken gap (or type-III) alignment between InAs and GaSb (after Ref. 9).

gap (misaligned, or type-III) band offsets between the GaSb/AlSb, InAs/AlSb, and InAs/GaSb material pairs, respectively, there is considerable flexibility in forming a rich variety of alloys and superlattices.

Basic properties of artificial material, InAs/GaSb T2SLs, supported by simple theoretical considerations are given by Ting *et al*. [5]. Their properties may be superior to those of the HgCdTe alloys and are completely different from those of constituent layers. The staggered band alignment of T2SL shown in Fig. 8(a) creates a situation in which the energy band gap of the superlattice can be adjusted to form either a semimetal (for wide InAs and GaInSb layers) or a narrow bandgap (for narrow layers) semiconductor material. The band gap of the SL is determined by the energy difference between the electron miniband E_1 and the first heavy hole state HH_1 at the Brillouin zone centre and can be varied continuously in a range between 0 and about 250 meV. One advantage of using type-II superlattice in LW and VLWIR is the ability to fix one component of the material and very the other to tune wavelength. An example of the wide tunability of the SLs shown in Fig. 8(b).

The SL band structure reveals important information about carrier transport properties. E_1 band shows strong dispersion along both the growth (z) and in-plane direction (x), whereas the HH_1 band is highly anisotropic and appears nearly dispersionless along the growth (transport) direction. The electron effective mass along the growth direction is quite small and even slightly smaller than in-plain electron effective mass. The values estimated by Ting *et al*. [5] for LWIR SL material (22 ML InAs/6 ML GaSb) are as follows: $m_e^{x*} = 0.023m_0$, $m_e^{z*} = 0.022m_0$, $m_{hh1}^{x*} = 0.04m_0$, and $m_{hh1}^{z*} = 1055m_0$. The SL conduction band structure near the zone centre is approximately isotropic in contrary to the highly anisotropic valence band structure. From this reasons we would expect very low hole mobility along the growth direction what is unfavourable in detector design for LWIR FPAs [25]. The estimation of effective masses for MWIR SL material (6 ML InAs/34 ML GaSb) gives [5]: $m_e^{x*} = 0.173m_0$, $m_e^{z*} = 0.179m_0$, $m_{hh1}^{x*} = 0.0462$, and $m_{hh1}^{z*} = 6.8m_0$ [5].
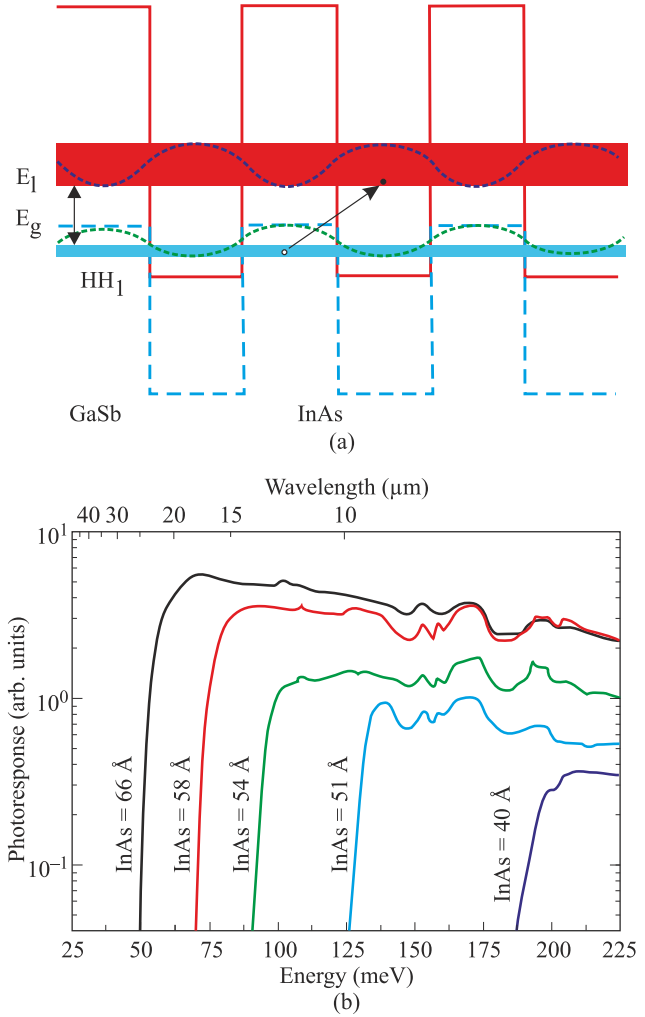

(a)

(b)

Fig. 8. InAs/GaSb strained layer superlattice: (a) band edge diagram illustrating the confined electron and hole minibands which form the energy bandgap; (b) experimental data of type-II SLS cutoff wavelengths change with the InAs thickness while GaSb is fixed at 40 Å (after Ref. 24).

The effective masses are not directly dependent on the band gap energy, as it is the case in a bulk semiconductor. The electron effective mass of InAs/GaSb SL is larger compared to $m_e^* = 0.009m_0$ in HgCdTe alloy with the same band gap ($E_g \approx 0.1$ eV). Thus, diode tunnelling currents in the SL can be reduced compared to the HgCdTe alloy. Although in-plane mobilities drop precipitously for thin wells, electron mobilities approaching 10^4 cm²/Vs have been observed in InAs/ GaSb SLs with the layers less than 40 Å thick.

In the 2TSL, the electrons are mainly located in the InAs layers, whereas holes are confined to the GaInSb layers. This suppresses Auger recombination mechanisms and thereby enhances carrier lifetime. Optical transitions occur spatially indirectly and, thus, the optical matrix element for such transitions is relatively small. Theoretical analysis of band-to--band Auger and radiative recombination lifetimes for InAs/ GaSb SLSs showed that Auger recombination rates are suppressed by several orders, compared to those of bulk HgCdTe with similar band-gap. However, the promise of Auger sup-

pression has not yet to be observed in a practical device material. At present time, the measured carrier lifetime is typically below 100 ns and is limited by Shockley-Read-Hall (SRH) mechanism in both MWIR and LWIR compositions. It is interesting to note that InSb, a member of III-V compound family, has had a similar SR lifetime issue since its inspection in 1950s. Recently, an increase in the minority carrier lifetime to 157 ns has been observed due to incorporation of InSb interfacial layer in InAs/GaSb 2TSL [26].

From the viewpoint of producibility, III-V materials offer much stronger chemical bonds and, thus higher chemical stability compared to HgCdTe. The 6.1 Å materials can be epitaxially grown on GaSb and GaAs substrates. In particular, 4-inch diameter GaSb substrates became commercially available in 2009 offering improved economy of scale for fabrication of large format FPAs arrays.

The most promising materials for barrier detector structures are InAs(InAsSb)/B-AlAsSb and InAs/GaSb T2SLs due to nearly zero VBO with respect to AlAsSb barriers. The InAsSb ternary alloy has a fairly weak dependence of the band edge on composition and is used in MWIR region. It was shown that by decreasing the valence band offset in InAsSb nBn devices, signal to noise ratio increases [18]. The InAs/GaSb T2SLs can be used as mid- or long-wavelength infrared absorber. In particular, the ability to tune the positions of the conduction band and valence band edges independently in the T2SL is especially helpful in the design of unipolar devices. This material system is in an early stage of development. Problems exist in material growth, processing, substrate preparation, and device passivation. Optimization of SL growth is a trade-off between interface roughness, with smoother interfaces at higher temperature, and residual background carrier concentrations, which are minimized on the low end of this range.

4. MWIR InAsSb barrier detectors

The detailed growth procedure and device's characterization of $InAs_{1-x}Sb_x/AlAs_{1-y}Sb_y$ nBn MWIR detector is described in several papers, e.g., Refs. 8, 9, 18, and 27. The n-type doping is usually reached by either Si or Te elements. The InAsSb structures were grown on either GaAs(100) or GaSb(100) substrates in a Veeco Gen200 MBE machine. The mismatched structures were grown on a 4-μm thick GaSb buffer layer, whereas the remaining structures were grown directly onto GaSb(100) substrates. The principal layers in the device structures were a thick n-type InAsSb absorption layer (1.5–3 μm), a thin n-type AlSbAs barrier layer (0.2–0.35 μm), and a thin (0.2–0.3 μm) n-type InAsSb contact layer. The bottom contact layer was highly doped.

Figure 9 shows an example of the similar nBn structure considered theoretically by Martyniuk and Rogalski [28] and the *I-V* characteristics as a function of temperature taken from Ref. 29. The alloy composition of $x = 0.195$ for the $InAs_{1-x}Sb_x$ absorber layer provided a cutoff wavelength ~ 4.9 μm at 150 K. J_{dark} is 1.0×10^{-3} A/cm^2 at 200 K and
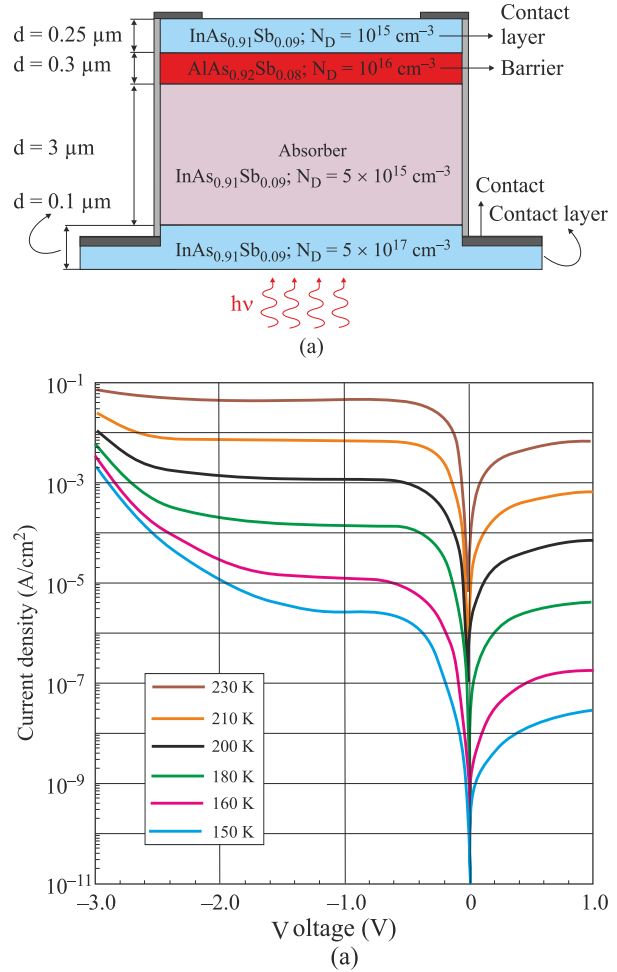

Fig. 9. InAsSb/AlAsSb nBn MWIR detector: the device structure (a) and dark current density *vs.* bias voltage as a function of temperature for 4096 (18 μm pitch) detectors ($\lambda_c \approx$ 4.9 μm at 150 K) tied together in parallel (after Ref. 29).

3.0×10^{-6} A/cm^2 at 150 K. The detectors are dominated by diffusion currents at –1.0 V bias where the quantum efficiency peaks.

Recently Klipstein *et al*. [17] have presented one of the first commercial nBn array detectors operated in the blue part of the MWIR window of the atmosphere (3.4–4.2 μm) and launched on the market by SCD. It is known as "Kinglet" and is a very low SWaP integrated detector cooler assembly (IDCA) with an aperture of F/5.5 and an operating temperature of 150 K. The complete IDCA has a diameter of 28 mm, length of 80 mm and weight of 300 gm; its power consumption is about 3 W at a 60 Hz frame rate [see Fig. 10(a)]. Kinglet digital detector based on SCD's Pelican-D ROIC contains a nBn $InAs_{0.91}Sb_{0.09}$/B-AlAsSb 640×512 pixels with a 15-μm pitch. The *NEDT* at optics F/3.2 and the pixel operability as a function temperature is shown in Fig. 10(b). The *NEDT* was 20 mK at 22 ms integration time, and the operability of non-defective pixels was greater than 99.5% after a standard two point non uniformity correction. The *NEDT* and operability begin to change above 170 K, what is consistent with the estimated BLIP temperature of 175 K.
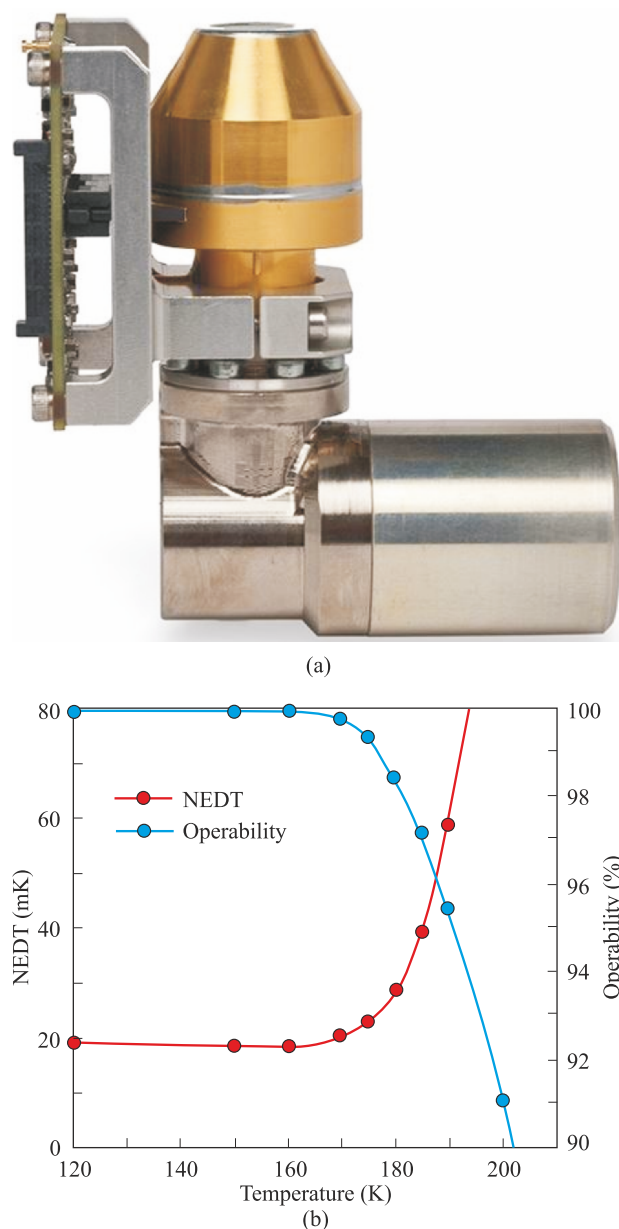
(a)

(b)

Fig. 10. The Kinglest detector: (a) photograph, and (b) temperature dependence of the NEDT (at optics F/3.2) and the pixel operability (after Ref. 17).

It should be mentioned, that recently a 1280×1024 nBn InAsSb FPA with 12-μm unit cells have been demonstrated by Lockheed Martin Santa Barbara Focal Plane and Teledyne Nova Sensors.

5. T2SL barrier detectors

Building unipolar barriers for InAs/GaSb superlattices is relatively straightforward because of the flexibility of the 6.1 Å III-V materials family – InAs, GaSb and AlSb. For SLs with the same GaSb layer widths, their valence band edges tend to line up very closely due to large heavy-hole mass. For this reason, an electron-blocking unipolar barrier for a given InAs/GaSb SL can be formed by using another InAs/GaSb SL with thinner InAs layers or a GaSb/AlSb SL.

The hole-blocking unipolar barriers are fabricated in different ways using complex supercells, such as the four-layer InAs/ GaInSb/ InAs/AlGaInSb "W" structure [30] and the four-layer GaSb/ InAs/GaSb/AlSb "M" structure [31]. Their designs is shown in Fig. 11. In "W" structure, two InAs electron-wells are located on either side of an InGaSb hole-well and are bound on either side by AlGaInSb barrier layers. The barriers confine the electron wavefunctions symmetrically about the hole-well, increasing the electron-hole overlap while nearly localizing the wavefunctions. The resulting quasi--dimensional densities of states give strong absorption near band edge. Due to flexibility in adjusting of "W" structure, this SL has been used as a hole-blocking unipolar barrier, an absorber, as well as an electron-blocking unipolar barrier.

In "M" structure [31,32], the wider energy gap AlSb-layer blocks the interaction between electrons in two adjacent InAs wells, thus, reducing the tunnelling probability and increasing the electron effective mass. The AlSb layer also acts as a barrier for holes in the valence band and converts the GaSb hole-quantum well into a double quantum well. As a result, the effective well width is reduced, and the hole's energy level becomes sensitive to the well dimension. This structure significantly reduces the dark current, and on the other hand, does not show any strong effect on the optical properties of the devices. Moreover, it has been proven its great flexibility in modifying the conduction and valence band energy levels [33]. As a result, FPAs for imaging in different IR regions, from SWIR to VLWIR can be fabricated [34].

In "N" structure [35] two monolayers of AlSb are inserted asymmetrically between InAs and GaSb layers, along the growth direction, as an electron barrier. This configuration increases electron-hole overlap under bias, significantly – consequently increasing the absorption while decreasing the dark current.

Table 2 illustrates some flat-band energy band diagrams and describes superlattice-based infrared detectors that make use of unipolar barriers including: double heterostruc-
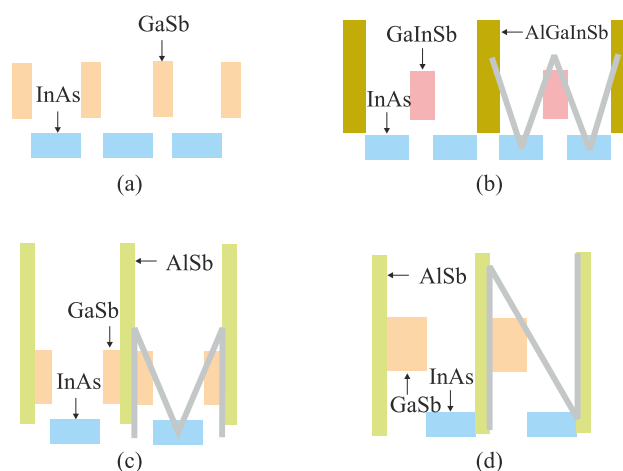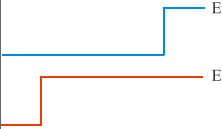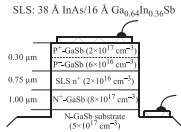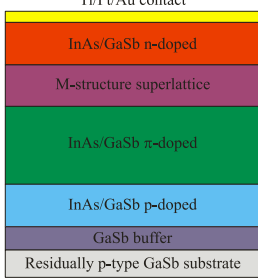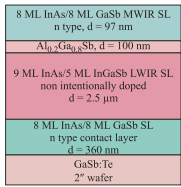

Fig. 11. Schematic energy band diagrams of (a) InAs/GaSb SL, (b) InAs/GaInSb/InAs/AlGaInSb "W" SL, (c) GaSb/InAs/GaSb/AlSb "M" SL, and (d) GaSb/InAs/AlSb "N" SL (adapted after Ref. 5).

Table 2. Type-II superlattice barrier detectors.

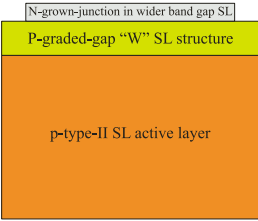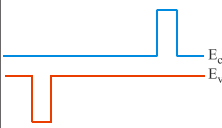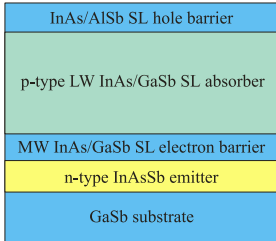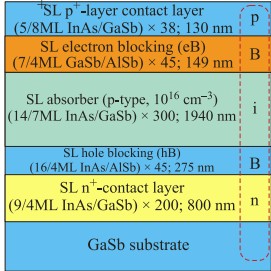| Flat-band energy diagrams	Examples	Description	Refs.
Double heterostructure	SLS: 38 Å InAs/16 Å Ga$_{0.64}$In$_{0.36}$Sb 0.30 µm P$^+$-GaSb (2×10^{17} cm^{-3}) P$^-$-GaSb (6×10^{16} cm^{-3}) 0.75 µm SLS n$^-$ type (2×10^{16} cm^{-3}) 1.00 µm N$^+$-GaSb (8×10^{17} cm^{-3}) N-GaSb substrate (5×10^{17} cm^{-3}) E_c E_v	**Double heterojunction (DH) photodiode** The first LWIR InAs/InGaSb SL DH photodiode grown on GaSb substrates with photoresponse out to 10.6 µm. The active region corresponding to n-type 39 Å InAs/16 Å Ga$_{0.65}$In$_{0.35}$Sb SL (2×10^{16} cm^{-3}) is surrounded by barriers made from p-GaSb and n-GaSb.	36
	Ti/Pt/Au contact InAs/GaSb n-doped M-structure superlattice InAs/GaSb π-doped InAs/GaSb p-doped GaSb buffer Residually p-type GaSb substrate	**p–π–M–n photodiode structure** The M structure is inserted between the π and n regions of a typical p-π-n structure. The T2SL part is chosen to have nominally 13 ML InAs and 7 ML GaSb for a cutoff wavelength of around 11 µm. The structure is designed with 18 ML InAs/3 ML GaSb/5 ML AlSb/3 ML GaSb for a cutoff wavelength of approximately 6 µm. In comparison with a standard p-π-n structure, the electric field in depletion region of p-π-M-n structure is reduced and the tunnelling barrier between the p and the n regions is spatially broadened. The structure consisted of a 250 nm thick GaS:Be p$^+$ buffer ($p \sim 10^{18}$ cm^{-3}), followed by a 500 nm thick InAs/GaSb:Be p$^+$ ($p \sim 10^{18}$ cm^{-3}) superlattice, a 2000 nm thick slightly p-type doped InAs:Be/GaSb region (π-region $p \sim 10^{18}$ cm^{-3}), a M-structure barrier, and a 500 nm thick InAs:Si/GaSb n$^+$ ($n \sim 10^{18}$ cm^{-3}) region, and topped with a thin InAs:Si n$^+$ doped ($n \sim 10^{18}$ cm^{-3}) contact layer.	31–34
Dual-band nBn E_c E_v	8 ML InAs/8 ML GaSb MWIR SL n type, d = 97 nm Al$_{0.2}$Ga$_{0.8}$Sb, d = 100 nm 9 ML InAs/5 ML InGaSb LWIR SL non intentionally doped d = 2.5 µm 8 ML InAs/8 ML GaSb SL n type contact layer d = 360 nm GaSb:Te 2″ wafer	**MWIR/LWIR nBn detector** In this dual-band SL nBn detector, the LWIR SL and MWIR SL are separated by AlGaSb unipolar barrier. The dual band response is achieved by changing the polarity of applied bias (see Fig. 12). The advantage of this structure is design simplicity and compatibility with commercially available readout integrated circuits. The concerns are connected with low hole mobility and lateral diffusion.	37
DH with graded-gap junction E_c E_v	N-grown-junction in wider band gap SL P-graded-gap "W" SL structure p-type-II SL active layer	**Shallow etch mesa isolation (SEMI) structure** It is n-on-p graded-gap "W" photodiode structure in which the energy gap is increased in a series of steps from that of the lightly p-type absorbing region to a value typically two to three times larger. The hole-blocking unipolar barrier is typically made from a four-layer InAs/GaInSb/InAs/AlGaInSb SL. The wider gap levels off about 10 nm short of the doping defined junction, and continues for another 0.25 µm into the heavily n-doped cathode before the structure is terminated by an n$^+$-doped InAs top cap layer. Individual photodiodes are defined using a shallow etch that typically terminates only 10 nm to 20 nm past the junction, which is sufficient to isolate neighbouring pixels while leaving the narrow-gap absorber layer buried 100–200 nm below the surface.	38,39
Complementary barrier E_c E_v	InAs/AlSb SL hole barrier p-type LW InAs/GaSb SL absorber MW InAs/GaSb SL electron barrier n-type InAsSb emitter GaSb substrate	**Complimentary barrier infrared detector (CBIRD)** This device consists of a lightly p-type InAs/GaSb SL absorber sandwiched between an n-type InAs/AlSb hole barrier (hB) SL and wider gal InAs/GaSb electron barrier (eB). The barriers are designed in a way to have approximately zero conduction and valence band offset with respect to SL absorber. A heavily doped n-type InAsSb layer adjacent to the eB SL acts as the bottom contact layer. The N-p junction between the hB InAs/AlSb SL and the absorber SL reduces SRH-related dark current and trap-assisted tunnelling. The LWIR CBIRD superlattice detector performance is closed to the "Rule 07" trend line. For a detector having a cutoff wavelength of 9.24 µm, the value of $R_0A > 10^5 \, \Omega \, cm^2$ at 78 K was measured.	9,40
	$^+$SL p$^+$-layer contact layer (5/8ML InAs/GaSb) × 38; 130 nm — p SL electron blocking (eB) (7/4ML GaSb/AlSb) × 45; 149 nm — B SL absorber (p-type, 10^{16} cm^{-3}) (14/7ML InAs/GaSb) × 300; 1940 nm — i SL hole blocking (hB) (16/4ML InAs/AlSb) × 45; 275 nm — B SL n$^+$-contact layer (9/4ML InAs/GaSb) × 200; 800 nm — n GaSb substrate	**pBiBn detector structure** This is another variation of the DH CBIRD structure. In this design a p-i-n photodiode is modified such that, there are unipolar electron barrier (eB) and hole barrier (hB) layers sandwiched between the p-contact layer and the absorber, and the n-contact layer and the absorber, respectively. This design facilitates a significant reduction in the electric field drop across the narrow-gap absorber region (most of the electric field drop across the wider bandgap eB and hB layers) what leads to a very small depletion region in the absorber layer, and hence reduction in the SRH, band-to-band tunnelling and trap-assisted-tunnelling current components.	41,42

ture (DH), dual band nBn structure, DH with graded gap junction and complementary barrier structure. As we can see, these structures are based on either the nBn/pBp/XBn architecture or different double heterostructure designs.

The first LWIR InAs/InGaSb SL double heterostructure photodiode grown on GaSb substrates with photoresponse out to 10.6 μm was described by Johnson *et al*. in 1996 [36]. In this structure the active SL region was surrounded by barriers made from p-GaSb and n-GaSb binary compounds. More recently, the barriers are also fabricated using different types of superlattices (see Table 2).

The realization of dual band detection capabilities with nBn design is schematically shown in Fig. 12 [5,43]. Under forward bias (defined as negative voltage applied on the top contact), the photocarriers are collected from the SL absorber with λ_2 cutoff wavelength. When the device is under reverse bias (defined as positive voltage applied on the top contact), the photocarriers from the SL absorber with λ_1 cutoff wavelength are collected, while those from the absorber with λ_2 cutoff wavelength are blocked by the barrier. Thus, the two-colour response is obtained under two different bias polarities.

Hood *et al*. [44] have modified the nBn concept to make the superior pBn LWIR device (see Fig. 3). In this structure, the p-n junction can be located at the interface between the heavily doped p-type contact material and the lower-doped barrier, or within the lower-doped barrier itself. Similar to nBn structure, the pBn structure still reduces *G-R* currents associated with SRH centres (the depletion region exists primarily in the barrier and does not appreciably penetrate the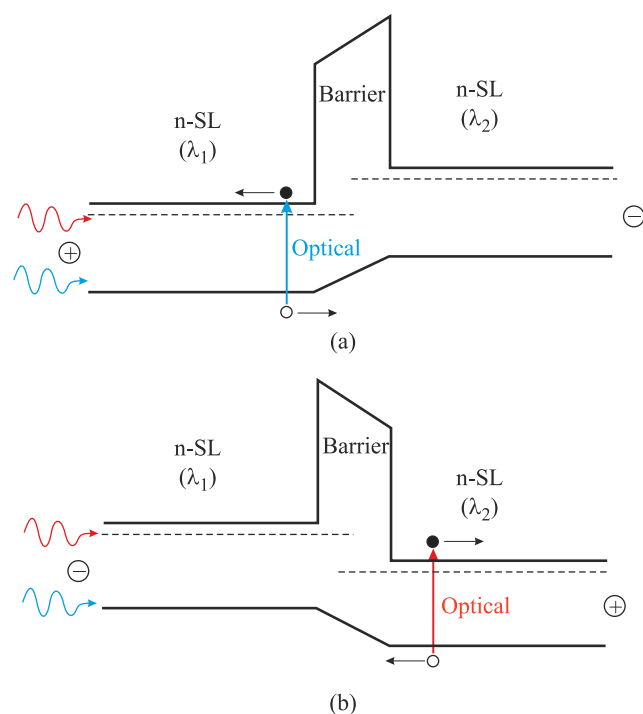 narrow-bandgap n-type absorber). In addition, the electric field in the barrier improves the response of the detector by sweeping from the active layer those photogenerated carriers that reach the barrier before they can recombine.

A variation of the DH detector structure is a structure with graded band gap in the depletion region. The graded gap region is inserted between the absorber and the hole barrier to reduce tunnelling and generation-recombination processes. The similar structure developed by The Naval Research Laboratory and Teledyne enables the shallow-etch mesa isolation (SEMI) structure for surface leakage current reduction. The junction is placed in the wider gap portion of the transition graded gap "W" layer. A shallow mesa etch just through the junction but not into the active layer isolates the diode, but still leaves a wide band gap surface for ease of passivation. A modest reverse bias allows for efficient collection from the active layer similar to planar double heterojunction p-on-n HgCdTe photodiodes [1].

However, a key feature of the devices is a pair of complementary barriers, namely, an electron barrier and a hole barrier formed at different depths in the growth sequence. Such structure is known as complementary barrier infrared device (CBIRD) and was invented by Ting and others at Jet Propulsion Laboratory. The device structure is shown inside of Table 2. An electron barrier (eB) appears in the conduction band and a hole barrier (hB) in the valence band. The two barriers complement one another to impede the flow of dark current. The absorber region, where the bandgap is smallest, is p-type and the top contact region is n-type, making an n-on-p polarity for the detector element. In sequence from the top, the first three regions are composed of superlattice material: the n-type cap, the p-type absorber, and the p-type eB. The highly doped n-InAsSb layer below the eB is an alloy. Further at the bottom are a GaSb buffer layer and the GaSb substrate.

The introduction of device designs containing unipolar barriers has taken the LWIR CBIRD superlattice detector performance close to the "Rule 07" trend line, which provides a heuristic predictor of the state-of-the-art HgCdTe photodiode performance [45]. The barriers prove to be very effective in suppressing the dark current. Figure 13 compares the I-V characteristics of a CBIRD device to a homojunction device made with the same absorber superlattice. Lower dark current determines higher *RA* product.

Usually, R_0A values are plotted for devices with near zero-bias turn-on. However, since the detector is expected to operate at a higher bias, a more relevant quantity is the effective resistance-area product. In the case of a detector having a cutoff wavelength of 9.24 μm, the value of $R_0A > 10^5\ \Omega\,cm^2$ at 78 K was measured, as compared with about 100 $\Omega\,cm^2$ for an InAs/GaSb homojunction of the same cutoff. For good photoresponse, the device must be biased to typically –200 mV; the estimated internal quantum efficiency is greater than 50%, while the RA_{eff} remains above $10^4\ \Omega\,cm^2$ [9].

Rhiger has gathered the 78 K dark current densities vs. detector cut-off wavelengths for nonbarrier (homojunction) and barrier (heterojunction) T2SL detectors reported in lit-
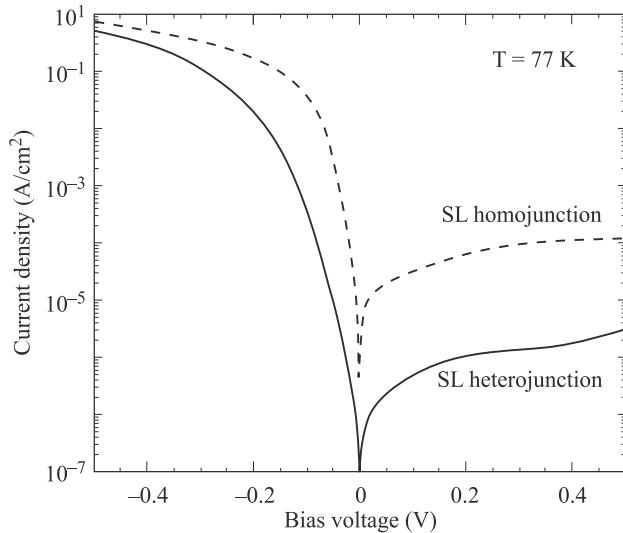

Fig. 12. Schematic band diagram for dual band nBn detector under (a) forward and (b) reverse bias.

Fig. 13. Dark *I–V* characteristics for a LWIR CBIRD detector and a superlattice homojunction at 77 K (after Ref. 5).
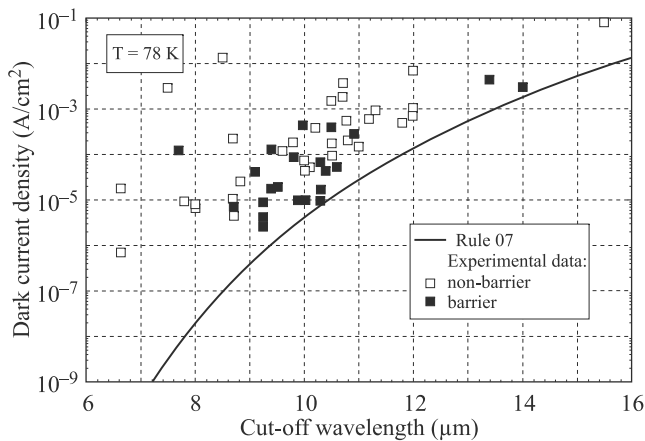

Fig. 14. The 78 K dark current densities plotted against cut-off wavelength for T2SL non-barrier and barrier detectors reported in the literature since late 2010. The solid line indicates the dark current density calculated using the empirical "Rule 07" model (after Ref. 46).
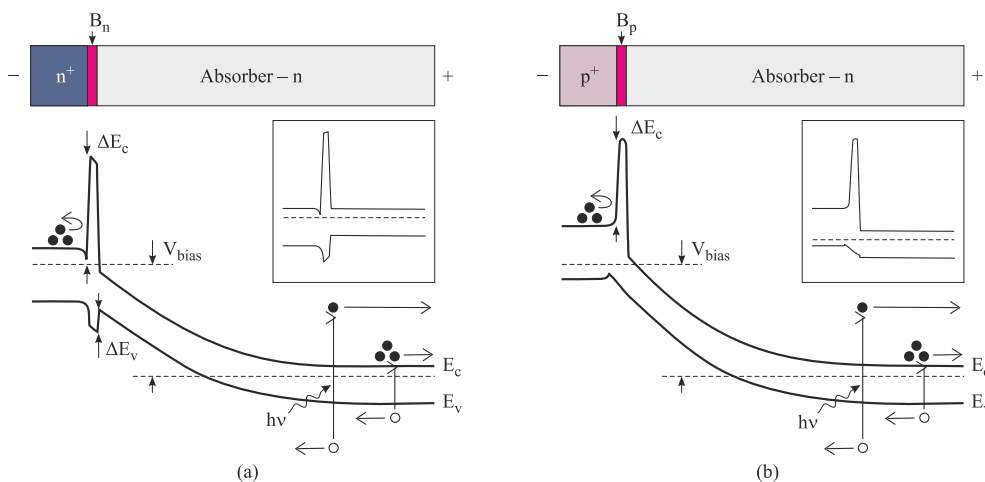
erature in the period since late 2010 (see Fig. 14) [46]. The nonbarrier dark currents are generally higher, with the best approaching "Rule 07" to within a factor of about 8. The barrier devices clearly show lower dark currents on average, and some are close to the curve Rule 07.

6. HgCdTe barrier detectors

The nBn architecture has been also implemented into HgCdTe, where technological successful attempts show a prospect for the circumventing of the p-type doping requirements in MBE technology. The HgCdTe nBn devices operating in MWIR range were presented by Itsuno *et al.* [47–49] and Kopytko *et al.* [50]. The HgCdTe ternary alloy is close to ideal infrared material system. Its position is conditioned by three key features: composition-dependent tailorable energy band gap, large optical coefficients that enable high quantum efficiency, and favourable inherent recombination mechanisms leading to long carrier lifetime and high operating temperature. In addition, an extremely small change of lattice constant with composition makes it possible to grow high quality layered structures and heterostructures. However, the existence of valence bans offset in HgCdTe-based nBn detectors [see Fig. 15(a)] creates several issues which limits the performance [51]. At low bias, the valence band barrier (ΔE_v) inhibits the minority carrier holes flow between the absorber and the contact cap layer. Depending on the wavelength of operation, a relatively high bias, typically greater than the bandgap energy is required to be applied to the device in order to collect all of the photogenerated carriers, which leads to strong band-to-band and trap-assisted tunnelling due to high electric field within the depletion layer.

First planar MWIR HgCdTe nB_nn structure with a 5.7 µm cut-off wavelength was grown on a bulk CdZnTe substrate in a Riber 32 MBE system [47]. The epitaxial nB_nn structure, shown in Fig. 15(a), consists of three indium doped n-type layers: a narrow bandgap cap, a wide bandgap barrier, and a narrow bandgap absorber. Uniform n-type doping ensures the absence of depletion in the narrow band-
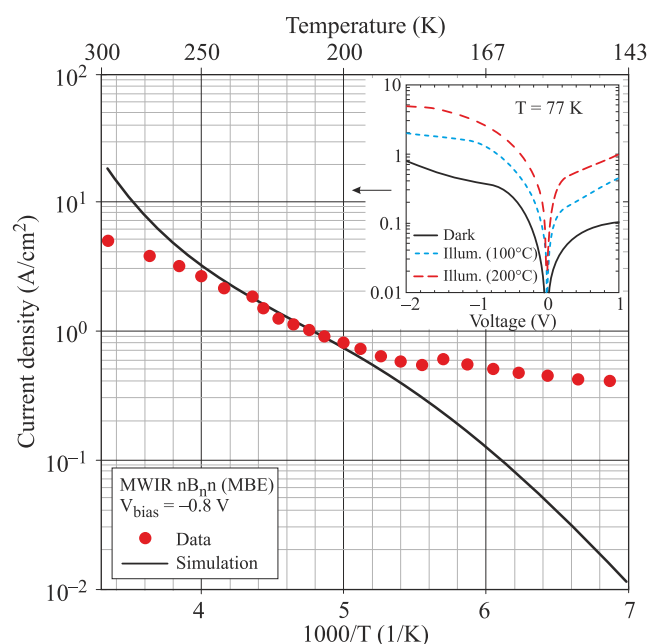

Fig. 15. Schematics energy band diagram of HgCdTe nB_nn (a) and pB_pn (b) detectors operating under illumination and reverse bias conditions.

Fig. 16. Current density at 0.8 V reverse bias as a function of temperature for MBE grown HgCdTe nB_nn detector. Inset: measured dark and unfiltered blackbody illuminated current-voltage characteristics at 77 K (after Ref. 47).

gap layers. Detector mesas were fabricated using plasma etching to access the absorber layer. Figure 16 presents the measured and calculated current density as a function of temperature. Within the temperature range between 180 K and 250 K, the dark current increases from 1 to 3 A/cm^2 and corresponds to the calculated model for a diffusion limit. Below 180 K, the experimental dark current saturates due to carrier generation via surface trap states along the sidewalls in the narrow bandgap absorber induced during the mesa etching.

The existence of the valence band barrier is still the main issue limiting the performance of HgCdTe nB_nn detectors. Its evidence is clearly evident in current-voltage characteristics where "turn-on" voltage values in the range of – 0.5 V to – 1.0 V. The "turn-on" bias range indicates the voltage required to align the valance band, enabling the collection of minority carrier holes from the absorber layer. Thus, present strategy in development of HgCdTe nBn detectors concentrates on decreasing or even removing the valence band offset in the barrier layer, what will result in lower operating bias, lower dark current, and ability to operate at higher temperatures. Ways to eliminated valence band offset have been proposed [52,53] and have been undertaken for HgCdTe barrier detectors by appropriate bandgap engineering [54].

One method to reduce the valence band offset is a proper p-type doping of the barrier. Such architecture is similar to that proposed by White in 1983, in which a p-type barrier is interposed between two narrow gap n-type regions [2]. Moreover, to reduce the "turn-on" voltage, an n-type contact cap layer might be replaced by a p-type contact without

affecting the dark current [8,10]. The p-n junction is then located at the barrier and absorber interface and its depletion region extends into the absorbing layer. The device with a p-type barrier and cap layer is shown in Fig. 17. The operation of the pB_pn device is similar to the operation of the nB_nn detector but does not require strong biasing.

As far as the uniform n-type doping of HgCdTe material is well understood in MBE method, controllable p-type doping requires inconvenient *ex situ* As-activation after formation of the detector structure. For that reason MOCVD growth seems to be more attractive. It allows to obtain *in situ* both donor and acceptor doping.

Recently, in a joint MOCVD laboratory run by Military University of Technology and VIGO System S.A., two type of HgCdTe barrier devices have been fabricated [55]. Both devices have the same cap-barrier structural unit (pB_p) and heavily doped bottom N$^+$-contact layer, but a different n- and p-type absorption layer. The epitaxial structures were grown in Aixtron AIX-200 MOCVD system on GaAs substrate with CdTe buffer layer. The schematic cross-section of the pB_pnN/pB_ppN mesa device is illustrated in Fig. 17. The detector mesas were fabricated by wet chemical etching with 4% bromine solution in glycol to the bottom contact (etch depth of about 7 μm). At the barrier-absorber and absorber-bottom contact layer interfaces is the *x*-graded region created by interdiffusion processes during Hg$_{1-x}$Cd$_x$Te growth at 350°C.
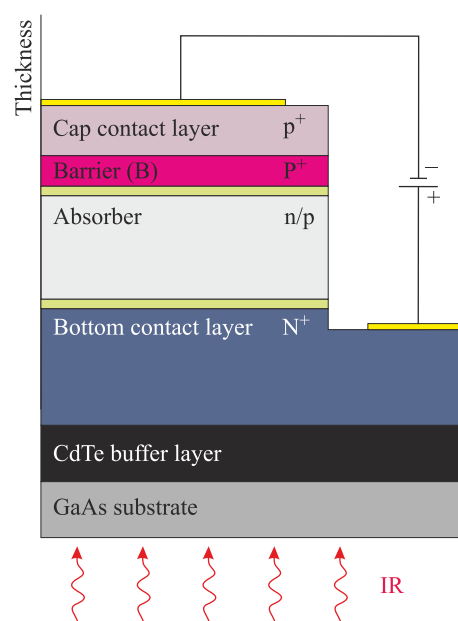

Fig. 17. MOCVD grown HgCdTe barrier photodetectors with mesa structure.

Figure 18 shows Arrhenius plots of the dark current at 0.25 V reverse biased pB_pnN and pB_ppN devices. The estimated thermal activation energy of about 0.33 eV for the device with n-type absorbing layer is close to the full Hg$_{0.64}$Cd$_{0.36}$Te bandgap, which in zero temperature equals 0.327 eV. This indicates diffusion limited dark currents.
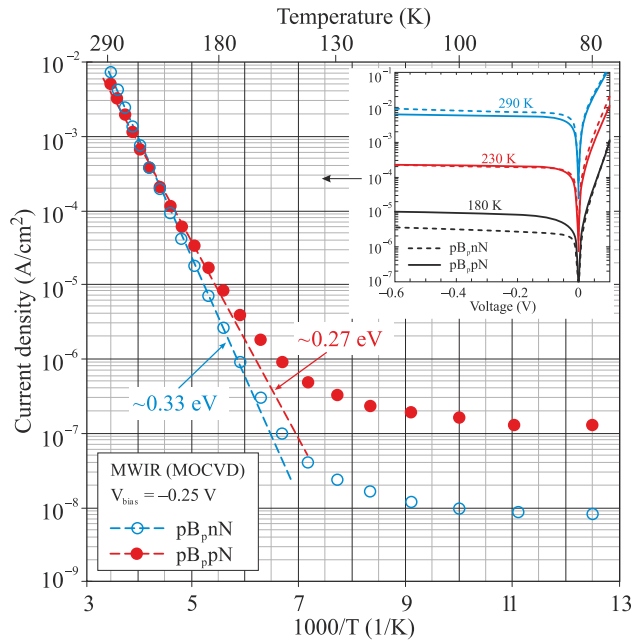
Fig. 18. Current density at 0.25 V reverse bias as a function of temperature for MOCVD grown pB$_n$nN and pB$_n$pN HgCdTe detectors. Inset: measured dark current-voltage characteristics at different operating temperatures (after Ref. 55).

The slope of about 0.27 eV for the device with p-type absorbing layer correspond to the activation energies for GR behaviour (about 0.8E_g). Below 120 K, both characteristics saturate reaching the dark current density equal 7.4×10^{-6} A/cm^2 for pB$_p$nN detector and more than one order of magnitude higher for pB$_p$pN photodiode.

Current-voltage characteristics show that the barrier detectors with pB$_p$ cap unit do not require a proper reverse bias ("turn-on voltage") to obtain the valence band alignment. It is also clearly visible on spectral characteristics presented in Fig. 19. Current responsivity of both devises (with n- and p-type absorbing layer) equalling 2 A/W is constant in the wide range of reverse bias voltage. Measured at 230 K spectral response curves show about 3.6 μm cut-off wavelength (at 50% of the initial rise in the response).

7. Imaging arrays

Figure 20 shows tremendous progress made in the past few years in the performance of type-II superlattice single element detectors or mini-arrays from USA major institutions: Northwestern University (NWU), Naval Research Laboratory (NRL), Jet Propulsion Laboratory (JPL), and Teledyne Imaging Scientific (TIS) [56]. This figure shows superlattice detector performance measured by dark current density as a multiple of "Rule 07" vs. time in years. The best SL device is within three times the value of HgCdTe "Rule 07". Most of the devices cited here have an absorber thickness of 2–4 μm, which limits its quantum efficiency to less than 40%. At the FPA level the dark current density is about one order of magnitude higher than that of single-element detectors, and within a factor of 20 of "Rule 07".
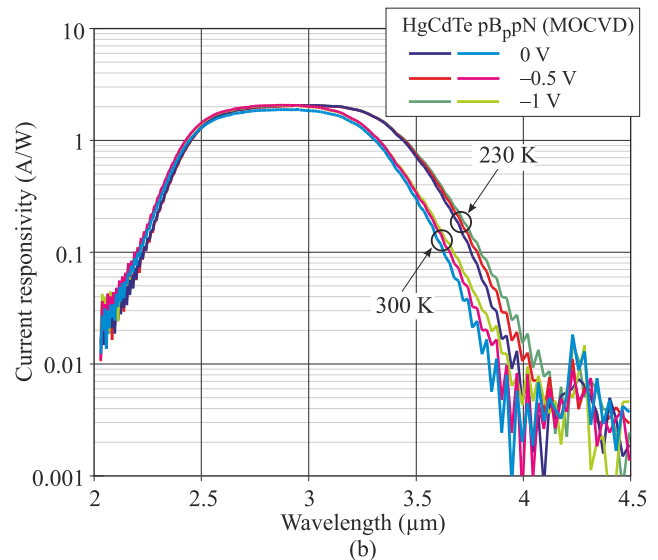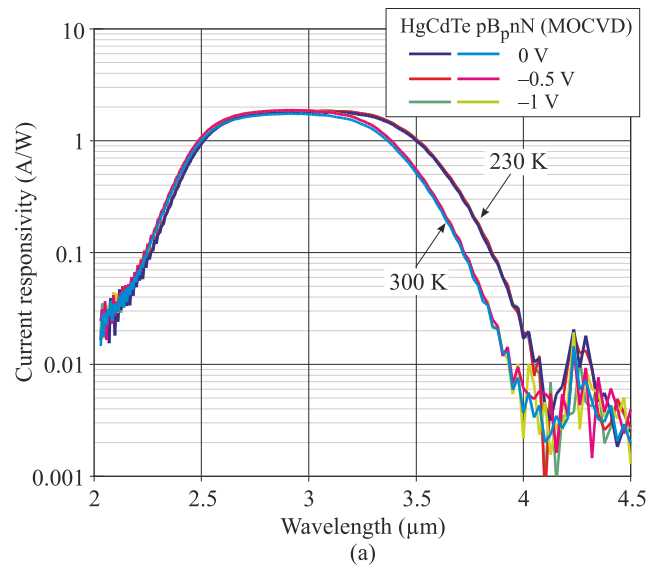

(a)

(b)

Fig. 19. Spectral current responsivity for MOCVD grown MWIR pB$_p$nN (a) and pB$_p$pN (b) HgCdTe detectors (after Ref. 55).

In the last three year the first megapixel MWIR and LWIR type-II SL FPAs have been demonstrated with an excellent imaging [57–59]. At about 78 K *NEDT* value below 20 mK has been presented for MW arrays; instead for LWIR – above 20 mK. Figure 21 presents imagers taken with MWIR 640×512 nBn array and two (MWIR and LWIR) megapixel photovoltaic arrays.

Multicolour capabilities are highly desirable for advance IR systems. Systems that gather data in separate IR spectral bands can discriminate both absolute temperature and unique signatures of objects in the scene. By providing this new dimension of contrast, multiband detection offers advanced colour processing algorithms to further improve sensitivity compared to that of single-colour devices. Recent trends in multi-spectral FPA development have leaned toward integrating multi-band functionality into single pixel, rather than combining multiple single-spectral arrays which requires spectral filters and spectrometers.
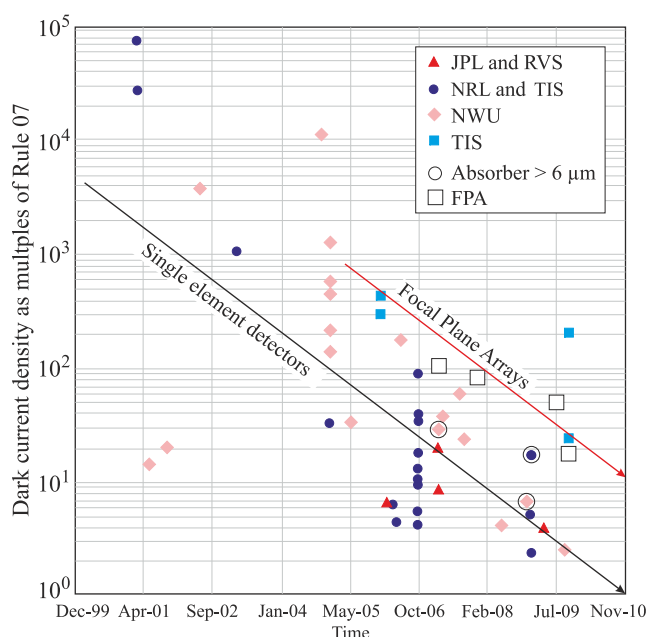
Fig. 20. Detector dark current density as a multiple of "Rule 07". The black line is drawn as an eye aid to show the trend line of dark current reduction along time for single element-detector, and the red line helps to show the trend for FPAs (after Ref. 56).
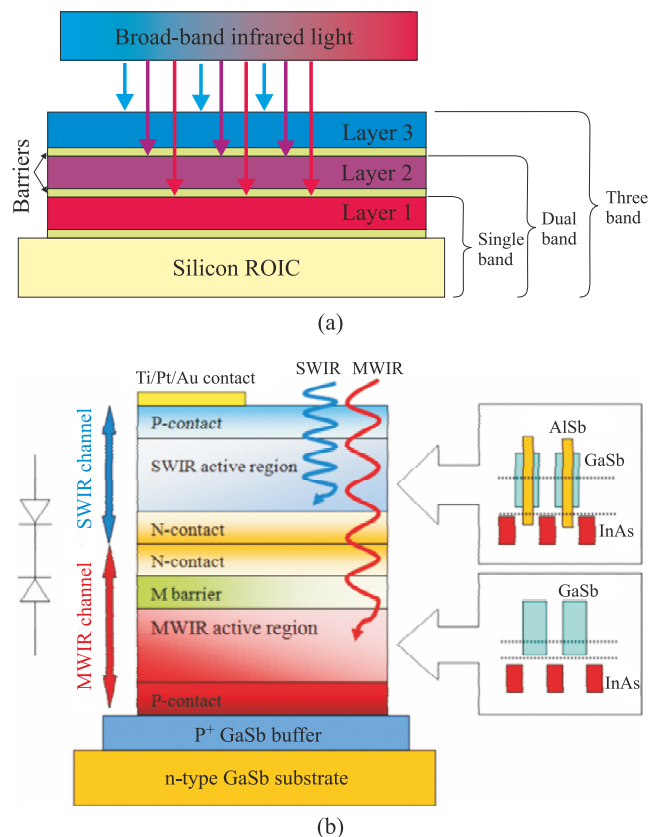

(a)

(b)

Fig. 22. Multi-colour detector pixels: (a) structure of a three-colour detector pixel. IR flux from the first band is absorbed in layer 3, while longer wavelength flux is transmitted through the next layers. The thin barriers separate the absorbing bands; (b) dual-band SW/MW InAs/GaSb/AlSb T2SL back-to-back p-i-n-n-i-p photodiode structure and schematic band alignment of superlattices in two absorption layers (dotted lines represent the effective band gaps of superlattices) (after Ref. 61).

Apart from HgCdTe photodiodes and QWIPs, T2SL material system has emerged as a candidate suitable for multi-spectral detection due to its ease in bandgap tuning, while retaining closely-matched conditions [60]. Three basic approaches to achieving multicolour detection have been proposed: multiple leads, voltage switched and voltage tuned. They are shortly described in chapter 16 of Rogalski's monograph [1].

Usually, the unit cell of integrated multicolour FPAs consists of several co-located detectors, each sensitive to a different spectral band (see Fig. 22). Radiation is incident on the shorter band detector, with the longer wave radiation passing through to the next detector. Each layer absorbs radiation up to its cutoff, and hence is transparent to the longer wavelengths, which are then collected in subsequent

layers. The device architecture is realized by placing a longer wavelength detector optically behind a shorter wavelength detector.

Research group of the Northwestern University has demonstrated different types of bias-selectable dual-band
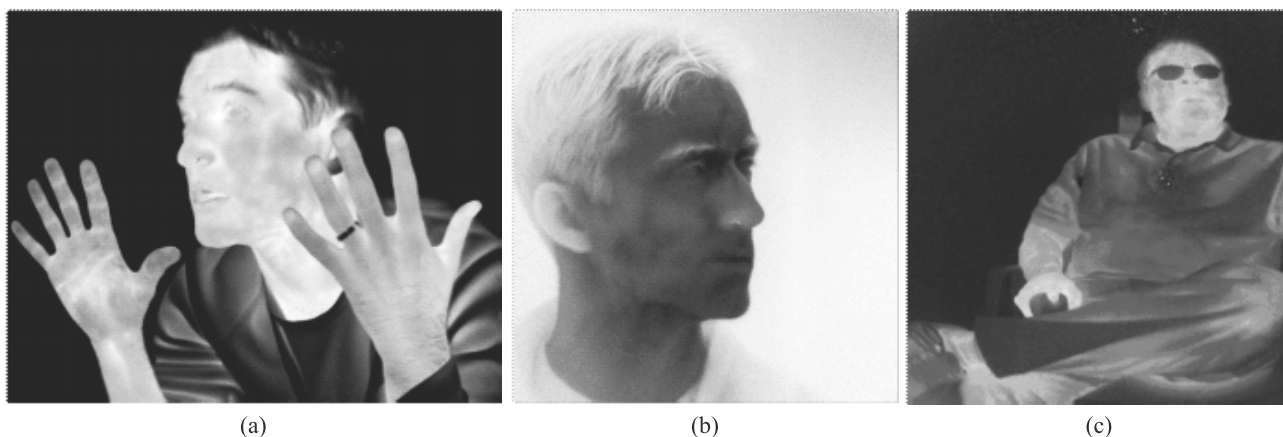

(a)

(b)

(c)

Fig. 21. Images taken with nBn 640×512 MWIR FPA (a), megapixel MWIR (b) and LWIR (b) Sb-based photovoltaic FPAs (after Refs. 57 and 58).

T2SL FPAs including combination of SW/MW, MW/LW, and LW1/LW2 arrays [34,61–63]. Figure 22(b) presents the schematic diagram of a dual-band SW/MW back-to-back p-i-n-n-i-p photodiode structure together with band alignment of superlattices in two absorption layers.

In the case of MW/LW back-to-back n-M-π-p-p-π-M-n structure, the MW active region was achieved by using 7.5 mono-layers (MLs) of InAs and 10 MLs of GaSb per period with the doping M-barrier. In the LW active region, 13 MLs of InAs and 7 MLs of GaSb were used in superlattice periods. The n-type GaSb semitransparent substrate was mechanically lapped down to 30–40 μm thickness and polished to a mirror-like surface. Figure 23(a) shows the detectivity spectrum of both MW and LW channels at 77 K. The *RA* product of LW channel at bias voltage of 0.2 V attained value close to 600 Ω cm². Median *NEDT* of ~10 mK and ~ 30 mK were achieved using 10 ms and 0.18 ms integration times for MW and LW channels, respectively. The imagery is seen in Fig. 23(b).

8. III–V barrier detectors vs. HgCdTe photodiodes

The nBn detectors are designed to reduce dark current associated with SRH processes and to decrease influence of surface leakage current without impending photocurrent (signal). In consequence, absence of a depletion region in barrier detectors offers a way to overcome the disadvantage of large depletion dark currents. So, they are typically implemented in materials with relatively poor SR lifetimes, such as all III-V compounds.

The band gap structure and physical properties of III-V compounds are found to be remarkably similar to HgCdTe with the same bandgap. It is interested to compare the dark currents generated within the detector absorber region composed of III-V and HgCdTe material systems.

The dark diffusion current density generated in absorber region is given by

$$J_{dark} = qGt, \qquad (1)$$

where q is the electron charge, G is the thermal generation rate in the base region, and t is the thickness of active region. Assuming that the thermal generation is a sum of Auger 1 and Shockley-Read mechanisms [64]

$$G = \frac{n_i^2}{N_d \tau_{A1}} + \frac{n_i^2}{(N_d + n_i)\tau_{SR}}, \qquad (2)$$

and that $\tau_{A1} = 2\tau_{A1}^t / [1 + (N_d / n_i)^2]$, the dark current density of n-type absorber region is

$$J_{dark} = \frac{qN_d t}{2\tau_{A1}^i} + \frac{qn_i^2 t}{(N_d + n_i)\tau_{SR}}. \qquad (3)$$

In the above equations, n_i is the intrinsic carrier concentration, N_d is the absorber doping level, and τ_{A1}^i is the intrinsic Auger 1 lifetime. From Eq. (3) results that the contribu-
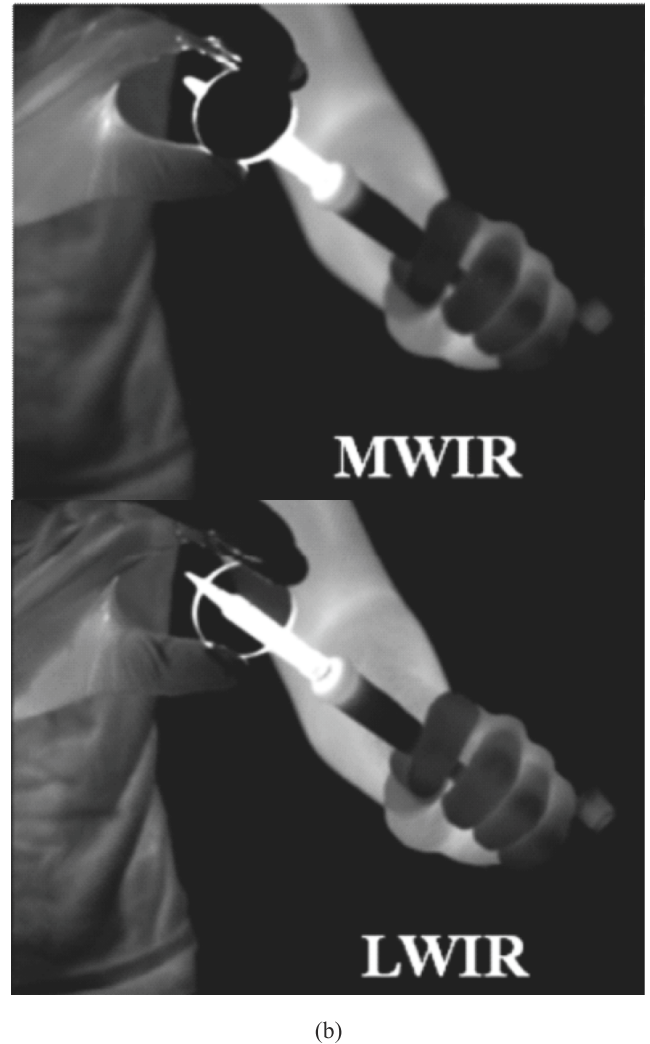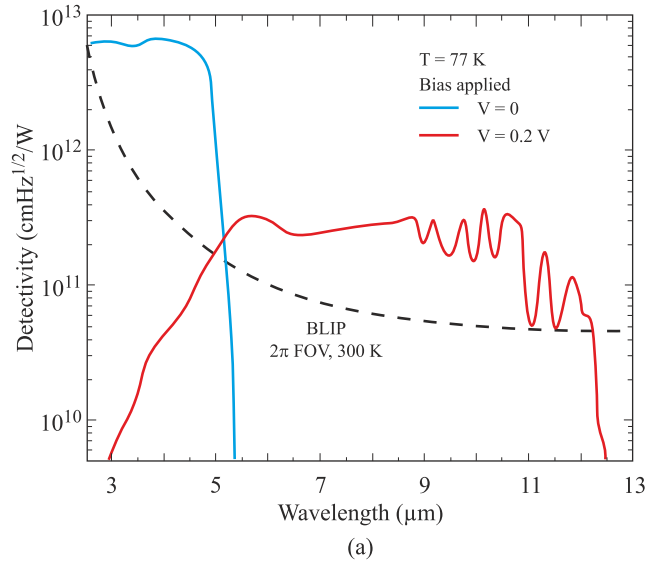

(a)

(b)

Fig. 23. Bias selectable dual-band MW/LW T2SL array: (a) detectivity spectrum of both MWIR and LWIR channels at 77 K shown with BLIP detectivity limit (2π FOV, 300 K background), (b) MWIR and LWIR channels imaging of a 11.3 μm narrow-band optical filter at 81 K (after Ref. 63).
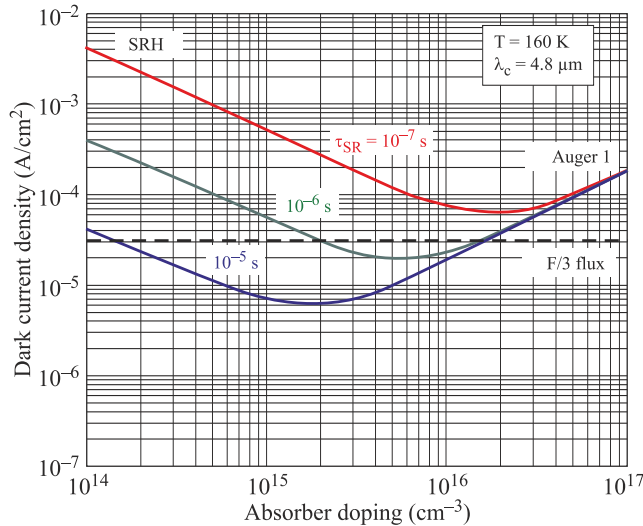
Fig. 24. Dependence of absorber dark current density on doping concentration for various values of SR lifetime at an operating temperature of 160 K and a cut-off wavelength of 4.8 μm, operating at an F/3 background flux (after Ref. 64).

tion of Auger 1 generation varies as *N*, whereas the SR generation varies as 1/*N*. As a result, the minimum dark current density depends on absorber doping concentration and on the value of SR lifetime, what is shown in Fig. 24. To approach BLIP performance, the detector with a 4.8-μm cut-off wavelength operating at 160 K with F/3 optics requires a generic IR material SR lifetime about 1 μs and optimized absorber doping of ~ 10^{16} cm^{-3}. A value of 0.6 μs, relatively independent of temperature, for τ_{SR} has been suggested in Ref. 64.

Figure 25 compares the predicted dependence of dark current density on operating temperature for different types of detectors with a 3-μm thick absorber and a cut-off wavelength of 4.8 μm [64]. In comparison with InAsSb photodiode (with built-in depletion region), the benefits of the
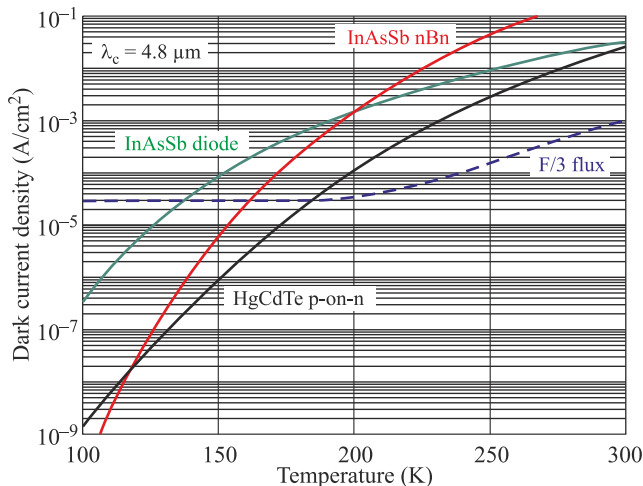
nBn structure is clear since it allows for operation at considerably higher temperatures. However, the HgCdTe photodiode enables higher operating temperatures than the InAsSb nBn detector by ~20 K. The best MWIR III-V devices are heavily doped, when the Auger lifetime is significantly reduced. 300-K data from Bewley *et al*. [65] show that Auger coefficients of SL devices are 5–20× lower than those of HgCdTe. To attain their full potential, the detector developers need to realize Auger-limited devices at doping in the 10^{15} cm^{-3} range. It should be stated that both III-V and HgCdTe MWIR detector architectures fall short of the ultimate performance possible with an F/3 optics, namely operation at about 150 K [see also Fig. 27(b)].

Theoretically, LWIR T2SL materials have lower fundamental dark currents than HgCdTe. Their performance has not achieved theoretical values. This limitation appears to be due to two main factors: relatively high background concentrations (about 10^{16} cm^{-3}), and a short minority carrier lifetime (typically tens of nanoseconds). Up until now non--optimized carrier lifetimes limited by Shockley–Read recombination mechanism have been observed. The minority carrier diffusion length is in the range of several micrometers. Improving these fundamental parameters is essential to realize the predicted performance of type-II photodiodes.

To date, LWIR T2SL photodiodes perform slightly worse than HgCdTe. For example, Figure 26 compares the predicted dependence of dark current density on operating temperature for InAs/GaSb pBp and HgCdTe photodiode with a cut-off wavelength of 10 μm [64]. The BLIP performance with F/1 optics for HgCdTe photodiode is achieved at about 130 K, about 15 K higher than for InAs/GaSb pBp detector.

The noise equivalent difference temperature (*NEDT*) can be determined knowing the dark current density, J_{dark}, the background flux (system optics), ϕ_B, and integration time, τ_{int}, according to relations [66]

Fig. 25. Comparison of dark current density *vs.* temperature for InAsSb photodiode and nBn detector and HgCdTe p-on-n photodiode with a cut-off wavelength of 4.8 μm.
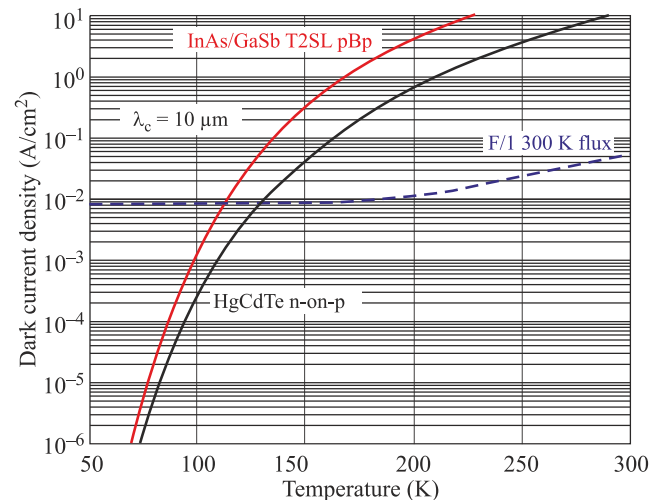

Fig. 26. Comparison of dark current density *vs.* temperature for InAs/GaSb T2SL pBp detector and HgCdTe n-on-p photodiode with a cut-off wavelength of 10 μm.

$$NEDT = \frac{1 + J_{dark}/J_B}{\sqrt{N}\left(\dfrac{1}{\phi_B}\dfrac{d\phi_B}{dT}\right)}, \qquad (4)$$

$$J_B = q\eta\phi_B, \qquad (5)$$

$$\sqrt{N} = \frac{(J_{dark} + J_B)\tau_{int}}{q}, \qquad (6)$$

where N is the well capacity of readout, $J_B = \eta\phi_B A_d$ is the background flux current, and A_d is the detector area.

Figure 27 shows the temperature dependence of the *NEDT* for barrier detectors and HgCdTe photodiodes with a cut-off wavelength of 4.8 μm and 10 μm [67]. In low temperature range the figure of merit of both material systems provide similar performance because they are predominantly limited by the readout circuits.
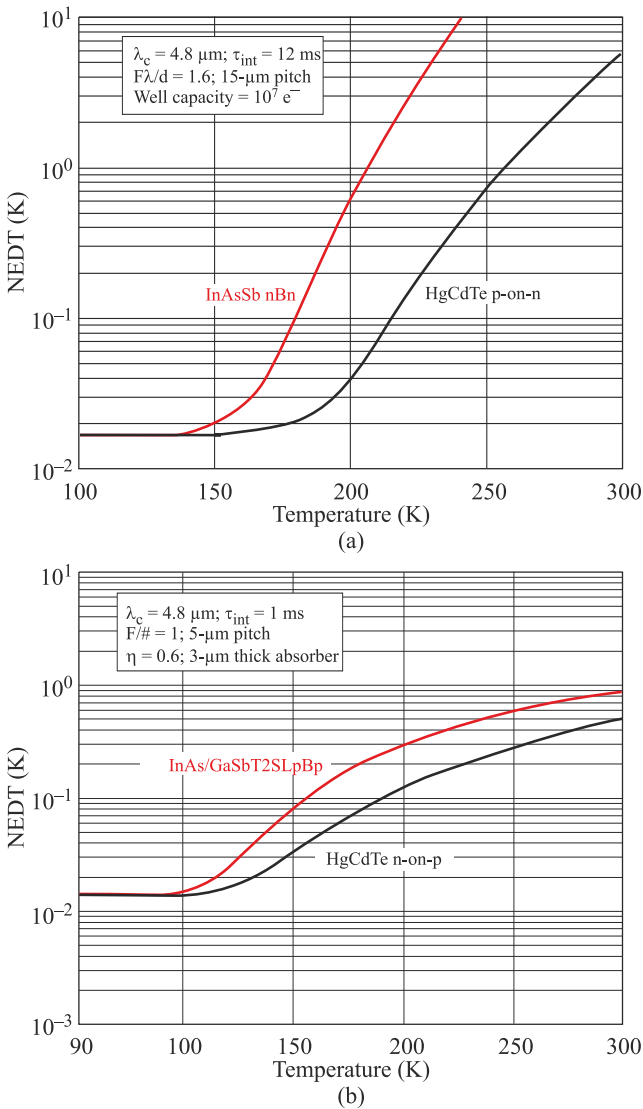

Fig. 27. Temperature dependence of the NEDT for barrier detectors and HgCdTe photodiodes with a cut-off wavelength of 4.8 μm (a) and 10 μm (b) (after Ref. 67).

Figure 28 compares the performance of optically immersed MWIR photovoltaic HgCdTe detectors with the, InAsSb, InAs/GaSb T2SLs and HgCdTe nBn HOT detectors. Properly designed, optically immersed HgCdTe devices (green solid line) approach BLIP limit (for 2π FOV) when are thermoelectrically (TE) cooled with 2-stage Peltier coolers. In this case the detectivity is proportional to n^2, where n is the refractive index equalling 3.4 for GaAs substrates/lenses. Without optical immersion MWIR HgCdTe photovoltaic detectors are sub-BLIP devices.

The detectivity for nBn T2SLs InAs/GaSb (10 ML/10 ML) and B-Al$_{0.2}$Ga$_{0.8}$Sb is presented for T = 300 K. The maximum D^* = 4×10^8 cmHz$^{1/2}$/W and quantum efficiency 15% were estimated [68]. D^* = 2×10^9 cmHz$^{1/2}$/W was reported for nBn InAsSb/AlAsSb detectors [28]. nBn and complementary barrier HgCdTe detectors operating in the MWIR range at T = 200 K reach detectivity of 6×10^9 and 2×10^{10} cmHz$^{1/2}$/W, respectively [51].

From considerations presented above result that despite numerous advantages of III-V barrier detectors over present-day detection technologies, including reduced tunnelling and surface leakage currents, normal-incidence absorption, and suppressed Auger recombination, the promise of superior performance of these detectors has not been yet realized. The dark current density is higher than that of bulk HgCdTe photodiodes, especially in MWIR range. To attain their full potential, the following essential technological limitations such as short carrier lifetime, passivation, and heterostructure engineering, need to be overcome.
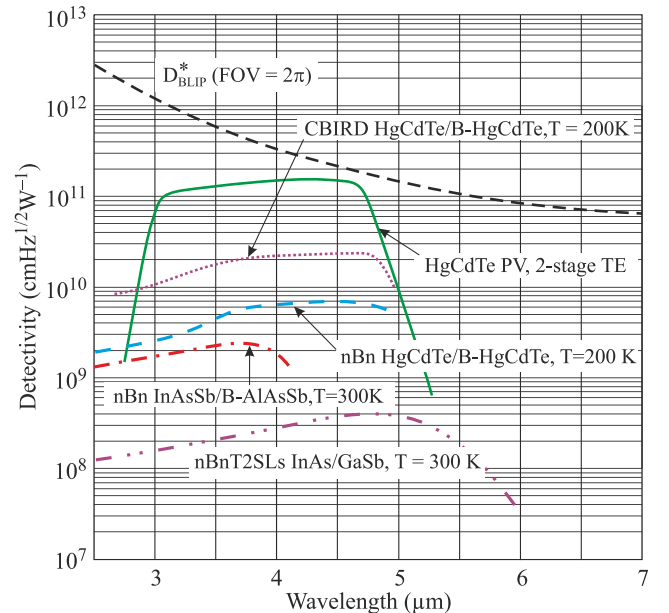

Fig. 28. Comparison of spectral detectivity of optically immersed MWIR photovoltaic HgCdTe detector (green line after Ref. 69) with different types of XBn detectors: nBn T2SLs InAs/GaSb and nBn InAsSb/B-AlAsSb operated at T = 300 K; and nBn HgCdTe/B-HgCdTe and complementary barrier HgCdTe detectors operated at T = 200 K.

9. Conclusions

It is predicted that in IR region HgCdTe technology will continue in the future to expand the envelope of its capabilities because of its excellent properties. Despite serious competition from alternative technologies, HgCdTe is unlikely to be seriously challenged for high-performance applications, applications requiring multispectral capability and fast response. However, the non-uniformity is a serious problem in the case of LWIR and VLWIR HgCdTe detectors. For applications that require operation in the LWIR band as well as two-colour MWIR/LWIR/VLWIR bands, most probably HgCdTe will not be the optimal solution. Type II InAs/GaInSb superlattice structure is a relatively new alternative IR material system and has great potential for LWIR/VLWIR spectral ranges with performance comparable to HgCdTe with the same cutoff wavelength. The fact that Sb-based superlattices are processed close to standard III-V technology raises the potential to be more competitive due to lower costs in series production.

A new strategies in photodetector designs include barrier detectors and unipolar barrier photodiodes. It seems to be clear that certain of these solutions have merged as a real competitions of HgCdTe photodetectors. The superior performance of barrier detector in comparison to conventional p-n junction photodiode is due to fact that the nBn structure is not limited by generation-recombination and tunnelling currents.

Absence of a depletion region in barrier detectors offers a way to overcome the disadvantage of large depletion dark currents. So, they are typically implemented in materials with relatively poor SR lifetimes, such as all III-V compounds. At present stage, theoretical predictions place T2SLs InAs/GaSb in front of the IR systems' development. In addition, fully developed III-V material technology and better stability over large area favour bulk materials for HOT conditions in MWIR range (e.g., InAsSb ternary alloy). Being grown on the GaAs/GaSb substrates, these $A^{III}B^V$ material systems are promising for the future integration with Si technology.

Despite numerous advantages of III-V barrier detectors over present-day detection technologies, the promise of superior performance of these detectors has not been yet realized. The dark current density is higher than that of bulk HgCdTe photodiodes, especially in MWIR range. To attain their full potential, the following essential technological limitations such as short carrier lifetime, passivation, and heterostructure engineering, need to be overcome.

Further strategy in development of barrier detectors should be also concentrated on decreasing or even removing the valence band offset in the barrier layer (especially in HgCdTe nBn detectors), what will result in lower operating bias, lower dark current, and ability to operate at higher temperatures. Ways to eliminate valence band offset have been proposed and have been undertaken for HgCdTe barrier detectors by appropriate bandgap engineering.

References

1. A. Rogalski, *Infrared Detectors*, 2nd edition, CRC Press, Boca Raton, 2010.
2. A. White, "Infrared detectors", U.S. Patent 4,679,063, 1983.
3. P.C. Klipstein, "Depletionless photodiode with suppressed dark current and method for producing the same", U.S. Patent 7,795,640, 2003.
4. S. Maimon and G. Wicks, "nBn detector, an infrared detector with reduced dark current and higher operating temperature", *Appl. Phys. Lett.* 89, 151109–1–3 (2006).
5. D.Z.-Y. Ting, A. Soibel, L. Höglund, J. Nguyen, C.J. Hill, A. Khoshakhlagh, and S.D. Gunapala, "Type-II superlattice infrared detectors", in *Semiconductors and Semimetals*, Vol. **84**, pp. 1–57, edited by S.D. Gunapala, D.R. Rhiger, and C. Jagadish, Elsevier, Amsterdam, 2011.
6. J.B. Rodriguez, E. Plis, G. Bishop, Y.D. Sharma, H. Kim, L.R. Dawson, and S. Krishna, "nBn structure based on InAs/GaSb type-II strained layer superlattices", *Appl. Phys. Lett.* **91**, 043514-1–2 (2007).
7. G.R. Savich, J.R. Pedrazzani, D.E. Sidor, and G.W. Wicks, "Benefits and limitations of unipolar barriers in infrared photodetectors", *Infrared Physics & Technol.* **59**, 152–155 (2013).
8. P. Klipstein, "XBn barrier photodetectors for high sensitivity operating temperature infrared sensors" *Proc. SPIE.* **6940**, 69402U-1–11 (2008).
9. D.Z. Ting, C.J. Hill, A. Soibel, J. Nguyen, S.A. Keo, M.C. Lee, J.M. Mumolo, J.K. Liu, and S.D. Gunapala, "Antimonide-based barrier infrared detectors", *Proc. SPIE* **7660**, 76601R-1–12 (2010).
10. P. Klipstein, O. Klin, S. Grossman, N. Snapi, I. Lukomsky, D. Aronov, M. Yassen, A. Glozman, T. Fishman, E. Berkowicz, O. Magen, I. Shtrichman, and E. Weiss, "XB*n* barrier photodetectors based on InAsSb with high operating temperatures" *Opt. Eng.* **50**, 061002-1–10 (2011).
11. G.R. Savich, J.R. Pedrazzani, D.E. Sidor, S. Maimon, and G.W. Wicks, "Use of unipolar barriers to block dark currents in infrared detectors" *Proc. SPIE* **8012**, 8022T (2012).
12. P. Martyniuk and A. Rogalski, "HOT infrared photodetectors", *Opto-Electron. Rev.* **21**, 240-258 (2013).
13. P. Klipstein, D. Aronov, E. Berkowicz, R. Fraenkel, A. Glozman, S. Grossman, O. Klin, I. Lukomsky, I. Shtrichman, N. Snapi, M. Yassem, and E. Weiss, "Reducing the cooling requirements of mid-wave IR detector arrys", *SPIE Newsroom* 10.1117/2.1201111.003919, 2011.
14. M. Razeghi, S.P. Abdollahi, E.K. Huang, G. Chen, A. Haddadi, and B.M. Nquyen, "Type-II InAs/GaSb photodiodes and focal plane arrays aimed at high operating temperatures", *Opto-Electr. Rev.* **19**, 261–269 (2011).
15. M. Razeghi, "Type II superlattice enables high operating temperature," *SPIE Newsroom*, 10.1117/2.1201110.003870 (2011).
16. G.R. Savich, J.R. Pedrazzani, D.E. Sidor, S. Maimon, and G.W. Wicks, "Dark current filtering in unipolar barrier infrared detectors", *Appl. Phys. Lett.* **99**, 121112 (2011).
17. P.C. Klipstein, Y. Gross, A. Aronov, M. ben Ezra, E. Berkowicz, Y. Cohen, R. Fraenkel, A. Glozman, S. Grossman, O. Kin, I. Lukomsky, T. Markowitz, L. Shkedy, I. Sntrichman, N. Snapi, A. Tuito, M. Yassen, and E. Weiss, "Low SWaP MWIR detector based on XBn focal plane array" *Proc. SPIE* **8704**, id. 87041S-1-12 (2013).

18. A. Khoshakhlagh, S. Myers , E. Plis , M.N. Kutty, B. Klein, N. Gautam, H. Kim, E.P.G. Smith, D. Rhiger, S.M. Johnson, and S. Krishna, "Mid-wavelength InAsSb detectors based on nBn design", *Proc. SPIE* **7660**, 76602Z (2010).

19. A.M. Itsuno, J.D. Philips, and S. Velicu, "Design and modelling of HgCdTe nBn detectors", *J. Elect. Mater.* **40**, 1624–1629 (2011).

20. M. Kopytko, A. Kębłowski, W. Gawron, P. Madejczyk, A. Kowalewski, and K. Jóźwikowski, "High-operating temperature MWIR nBn HgCdTe detector grown by MOCVD", *Opto-Electr. Rev.* **21**. 42, 402-405 (2013).

21. J.F. Klem, J.K. Kim, M.J. Cich, S.D. Hawkins, T.R. Fortune, and J.L. Rienstra, "Comparison of nBn and nBp mid-wave barrier infrared photodetectors", *Proc. SPIE* **7608**, 76081P (2010).

22. H. Kroemer, "The 6.1 Å family (InAs, GaSb, AlSb) and its heterostructures: a selective review", *Physica* **E20**, 196–203 (2004).

23. H. Sakaki, L.L. Chang, R. Ludeke, C.A. Chang, G.A. Sai-Halasz, and L. Esaki, "In$_{1-x}$Ga$_x$As-GaSb$_{1-y}$As$_y$ heterojunctions by molecular beam epitaxy", *Appl. Phys. Lett.* **31**, 211–213 (1977).

24. Y. Wei and M. Razeghi, "Modelling of type-II InAs/GaSb superlattices using an empirical tight-binding method and interface engineering", *Phys. Rev.* **B69**, 085316-7 (2004).

25. G.A. Umana-Membreno, B. Klein, H. Kala, J. Antoszewski, N. Gautam, M.N. Kutty, E. Plis, S. Krishna, and L. Faraone, "Vertical minority carrier electron transport in p-type InAs/GaSb type-II superlattices", *Appl Phys. Lett.* **101**, 253515 (2012).

26. D. Zuo, P. Qiao, D. Wasserman, and S.L. Chuang, "Direct observation of minority carrier lifetime improvement in InAs/GaSb type-II superlattice photodiodes via interfacial layer control", *Appl. Phys. Lett.* **102**, 141107 (2013).

27. E. Weiss, O. Klin, S. Grossmann, N. Snapi, I. Lukomsky, D. Aronov, M. Yassen, E. Berkowicz, A. Glozman, P. Klipstein, A. Fraenkel, and I. Shtrichman, "InAsSb-based XBnn barriodes grown by molecular beam epitaxy on GaAs", *J. Crystal Growth* **339**, 31–35 (2012).

28. P. Martyniuk and A. Rogalski, "Modelling of InAsSb/AlAsSb nBn HOT detector's performance limits", *Proc. SPIE* **8704**, 87041X (2013).

29. A.I. D'Souza, E. Robinson, A.C. Ionescu, D. Okerlund, T.J. de Lyon, R.D. Rajavel, H. Sharifi, N.K. Dhar, P.S. Wijewarnasuriya, and C. Grein, "5MWIR InAsSb barrier detector data and analysis", *Proc. SPIE* **8704**, 87041U (2013).

30. E.H. Aifer, J.G. Tischler, J. H. Warner, I. Vurgaftman, W.W. Bewley, J.R. Meyer, J.C. Kim, and L.J. Whitman, "W-structured type-II superlattice long-wave infrared photodiodes with high quantum efficiency", *Appl. Phys. Lett.* **89**, 053519 (2006).

31. B.-M. Nguyen, M. Razeghi, V. Nathan, and G.J. Brown, "Type-II "M" structure photodiodes: an alternative material design for mid-wave to long wavelength infrared regimes", *Proc. SPIE* **6479**, 64790S (2007).

32. B.-M. Nguyen, D. Hoffman, P.-Y. Delaunay, and M. Razeghi, "Dark current suppression in type II InAs/GaSb superlattice long wavelength infrared photodiodes with M-structure", *Appl. Phys. Lett.* 163511 (2007).

33. B.-M. Nguyen, D. Hoffman, P.-Y. Delaunay, E.K. Huang, M. Razeghi, and J. Pellegrino, "Band edge tunability of *M*-structure for heterojunction design in Sb based type II superlattice photodiodes", *Appl. Phys. Lett.* **93**, 163502 (2008).

34. M. Razeghi, H. Haddadi, A.M. Hoang, E.K. Huang, G. Chen, S. Bogdanov, S.R. Darvish, F. Callewaert, and R. McClintock, "Advances in antimonide-based Type-II superlattices for infrared detection and imaging at centre for quantum devices", *Infrared Phys. & Technol.* **59**, 41–52 (2013).

35. O. Salihoglu, A. Muti, K. Kutluer, T. Tansel, R. Turan, Y. Ergun, and A. Aydinli, "«N» structure for type-II superlattice photodetectors", *Appl. Phys. Lett.* **101**, 073505 (2012).

36. J.L. Johnson, L.A. Samoska, A.C. Gossard, J.L. Merz, M.D. Jack, G.H. Chapman, B.A. Baumgratz, K. Kosai, and S.M. Johnson, "Electrical and optical properties of infrared photodiodes using the InAs/Ga$_{1-x}$In$_x$Sb superlattice in heterojunctions with GaSb", *J. Appl. Phys.* **80**, 1116–1127 (1996).

37. A. Khoshakhlagh J.B. Rodriguez, E. Plis, G.D. Bishop, Y.D. Sharma, H.S. Kim, L.R. Dawson and S. Krishna, "Bias dependent dual band response from InAs/Ga(In)Sb type II strain layer superlattice detectors", *Appl. Phys. Lett.* **91**, 263504 (2007).

38. I. Vurgaftman, E.H. Aifer, C.L. Canedy, J.G. Tischler, J.R. Meyer, and J.H. Warner, "Graded band gap for dark-current suppression in long-wave infrared W-structured type-II superlattice photodiodes", *Appl. Phys. Lett.* **89**, 121114 (2006)

39. E.H. Aifer, J.H. Warner, C.L. Canedy, I. Vurgaftman, E.M. Jackson, J.G. Tischler, J.R. Meyer, S.P. Powell, K. Olver, and W.E. Tennant, "Shallow-etch mesa isolation of graded-bandgap''W''-structured type II superlattice photodiodes", *J. Electron. Mater.* **39**, 1070-1079 (2010).

40. D.Z.-Y. Ting, C.J. Hill, A. Soibel, S.A. Keo, J.M. Mumolo, J. Nguyen, and S.D. Gunapala, "A high-performance long wavelength superlattice complementary barrier infrared detector", *Appl. Phys. Lett.* **95**, 023508 (2009).

41. E.A. DeCuir, G.P. Meissner, P.S. Wijewarnasuriya, N. Gautam, S. Krishna, N.K. Dhar, R.E. Welser, and A.K. Sood, "Long-wave type-II superlattice detectors with unipolar electron and hole barriers", *Opt. Eng.* **51**, 124001 (2012).

42. N. Gautam, S. Myers, A.V. Barve, B. Klein, E.P. Smith, D. Rhiger, E. Plis, M.N. Kutty, N. Henry, T. Schuler-Sandyy, and S. Krishna, "Band engineering HOT midwave infrared detectors based on type-II InAs/GaSb strained layer superlattices", *Infrared Physics & Techol.* **59**, 72-77 (2013).

43. E. Plis, H.S. Kim, G. Bishop, S. Krishna, K. Banerjee, and S. Ghosh, "Lateral diffusion of minority carriers in nBn based type-II InAs/GaSb strained layer superlattice detectors", *Appl. Phys. Lett.* **93**, 123507 (2008).

44. A.D. Hood, A.J. Evans, A. Ikhlassi, D.L. Lee, and W.E. Tennant, "LWIR strained-layer superlattice materials and devices at Teledyne Imaging Sensors", *J. Electron. Mater.* **39**, 1001–1006 (2010).

45. W.E. Tennant, D. Lee, M. Zandian, E. Piquette, and M. Carmody, "MBE HgCdTe Technology: A very general solution to IR detection, described by 'Rule 07', a very convenient heuristic", *J. Electron. Mater.* **37**, 1406 (2008).

46. D.R. Rhiger, "Performance comparison of long-wavelength infrared type II superlattice devices with HgCdTe", *J. Electron. Mater.* **40**, 1815–1822 (2011).

47. A.M. Itsuno, J.D. Phillips, and S. Velicu, "Mid-wave infrared HgCdTe nBn photodetector", *Appl. Phys. Lett.* **100**, 161102 (2012).

48. A.M. Itsuno, J.D. Phillips, and S. Velicu, "Design of an Auger-suppressed unipolar HgCdTe NBnN photodetector", *J. Electron. Mater.* **41**, 2886–2892 (2012).

49. S. Velicu, J. Zhao, M. Morley, A.M. Itsuno, and J.D. Philips, "Theoretical and experimental investigation of MWIR HgCdTe nBn detectors", *Proc. SPIE* **8268**, 82682X-1-13 (2012).

50. M. Kopytko, A. Kębłowski, W. Gawron, P. Madejczyk, A. Kowalewski, and K. Jóźwikowski, "High-operating temperature MWIR nBn HgCdTe detector grown by MOCVD", *Opto-Electr. Rev.* **21**, 402-405 (2013).

51. P. Maryniuk and A. Rogalski, "Modelling of MWIR HgCdTe complementary barrier HOT", *Solid-State Electronics* **80**, 96–104 (2013).

52. E.F. Schubert, L.W. Tu. G.J. Zydzik, R.F. Kopf, A. Benvenuti and M.R. Pinto, "Elimination of heterojunction band discontinuities by modulation doping", *Appl. Phys. Lett.* **60**, 466-468 (1992).

53. S.D. Gunpala, D.Z Ting, C.J. Hill, and S.V. Bandara, *U.S. Patent* No. 7,737,411, 2010.

54. N.D. Akhavan, G. Jolley, G. Umana-Membreno, J. Antoszewski, and L. Faraone, "Performance modelling of bandgap engineered HgCdTe-based nBn infrared detectors", *Extended Abstracts*, *The 2013 Workshop on the Physics and Chemistry of II–VI Materials*, Chicago (2013).

55. M. Kopytko, A. Kębłowski, W. Gawron, A. Kowalewski, "MOCVD grown HgCdTe barrier structures for high-operating temperature MWIR photodetectors", to be published.

56. L. Zheng, M. Tidrow, L. Aitcheson, J. O'Connor, and S. Brown, "Developing high-performance III-V superlattice IRFPAs for defense – challenges and solutions", *Proc. SPIE* **7660**, 7660-1–12 (2010).

57. C.J. Hill, A. Soibel, S.A. Keo, J.M. Mumolo, D.Z. Ting, S.D. Gunapala, D.R. Rhiger, R.E. Kvaas, and S.F. Harris, "Demonstration of mid and long-wavelength infrared antimonide-based focal plane arrays", *Proc. SPIE* **7298**, 7294–04 (2009).

58. S.D. Gunapala, D.Z. Ting, C.J. Hill, J. Nguyen, A. Soibel, S.B. Rafol, S.A. Keo, J.M. Mumolo, M.C. Lee, J.K. Liu, and B. Yang, "Demonstration of a 1024×1024 pixel InAs-GaSb superlattice focal plane array", *Phot. Tech. Lett.* **22**, 1856–1858 (2010).

59. P. Manurkar, S. Ramezani-Darvish, B.-M. Nguyen, M. Razeghi, and J. Hubbs, "High performance long wavelength infrared mega-pixel focal plane array based on type-II superlattices", *Appl. Phys. Lett.* **97**, 193505-1–3 (2010).

60. A. Rogalski, J. Antoszewski, and L. Faraone, "Third-generation infrared photodetector arrays", *J. Appl. Phys.* **105**, 091101 (2009).

61. A.M. Hoang, G. Chen, A. Haddadi, and M. Razeghi, "Demnstration of high performance bias-selectable dual-band short-/mid-wavelength infrared photodetectors based on type-II InAs/GaSb/AlSb superlattices", *Appl. Phys. Lett.* **102**, 011108 (2013).

62. M. Razeghi, A.M. Hoang, A. Haddadi, G. Chen, S. Ramezani-Darvish, P. Bijjam, P. Wijewarnasuriya, and E. Decuir, "High-performance bias-selectable dual-band short-/Mid-wavelength infrared photodetectors and focal plane arrays based on InAs/GaSb/AlSb type-II superlattices", *Proc. SPIE* **8704**, 8704–54 (2013).

63. M. Razeghi, A. Haddadi, A.M. Hoang, G. Chen, S. Ramezani-Darvish, and P. Bijjam, "High-performance bias-selectable dual-band mid-/long-wavelength infrared photodetectors and focal plane arrays based on InAs/GaSb type-II superlattices", *Proc. SPIE* **8704**, 87040S (2013).

64. M.A. Kinch, H.F. Schaake, R.L. Strong, P.K. Liao, M.J. Ohlson, J. Jacques, C-F Wan, D. Chandra, R.D. Burford, and C.A. Schaake, "High operating temperature MWIR detectors", *Proc. SPIE* **7660**, 76602V-1 (2010).

65. W.W. Bewley, J.R. Lindle, C.S. Kim, M. Kim, C.L. Canedy, I. Vurgaftman, and J.R. Meyer, "Lifetime and Auger coefficients in type-II W interband cascade lasers", *Appl. Phys. Lett.* **93**, 041118 (2008).

66. M.A. Kinch, *Fundamentals of Infrared Detector Materials,* SPIE Press, Bellingham, 2007.

67. M.A. Kinch, "The challenges of background limited room temperature photon detection", *The 2013 U.S. Workshop on the Physics and Chemistry of II-VI Materials*, Tutorial Session, Chicago, 2013.

68. J. Wróbel, P. Martyniuk, E. Plis, P. Madejczyk, W. Gawron, S. Krishna, and A. Rogalski, "Dark current modeling of MWIR type-II superlattice detectors", *Proc. SPIE* **8353**, 8353–16 (2012).

69. http://www.vigo.com.pl/